Ghaderi Masouleh, M.; Keskinen, Karri; Kaario, O.; Kahila, H.; Karimkashi, S.; Vuorinen, V.

Modeling cycle-to-cycle variations in spark ignited combustion engines by scale-resolving simulations for different engine speeds

Published in:
Applied Energy

DOI:
10.1016/j.apenergy.2019.03.198

Published: 11/05/2019

Document Version
Publisher's PDF, also known as Version of record

Applied Energy 250 (2019) 801–820

Contents lists available at ScienceDirect

Applied Energy

journal homepage: www.elsevier.com/locate/apenergy

Modeling cycle-to-cycle variations in spark ignited combustion engines by scale-resolving simulations for different engine speeds

M. Ghaderi Masouleh[a], K. Keskinen[b], O. Kaario[a], H. Kahila[a], S. Karimkashi[a], V. Vuorinen[a]

[a] Aalto University, School of Engineering, Department of Mechanical Engineering, Finland
[b] Swiss Federal Institute of Technology Zürich (ETHZ), Switzerland

HIGHLIGHTS

- Cyclic variation is numerically investigated in a spark-ignited lean gas engine.
- The cyclic variations are explained using local flame analysis.
- Turbulence around the early flame front is the major contributor to the observed CCV.
- Flame kernel is more prone to local conditions when it is small.
- The higher the RPM, the longer the initial effects may persist in CAD time.

ARTICLE INFO

Keywords:
Cycle-to-cycle variation
Spark-ignited gas engine
Large-eddy simulation
Engine rotational speed
G-equation
Lean combustion

ABSTRACT

Here, internal combustion engine operating speed effects on combustion cycle-to-cycle variations (CCV) are numerically investigated. The recent study by Ghaderi Masouleh et al. (2018) is extended to higher engine speeds including 560, 800 and 1000 RPM. The 3D scale-resolving simulations are carried out in a spark ignited simplified engine geometry under fuel lean condition. The numerical results include the following main findings. (1) Flow velocity and turbulence levels are noted to increase with RPM. (2) For a fixed spark timing, the combustion duration in CAD time increases with RPM contrasting the respective trend in physical time. (3) The link between early flow conditions around the spark position and the whole cycle combustion rate is demonstrated and explained for all the RPM for the investigated three example cycles. (4) On average, the moderate increase of turbulent flame speed with RPM is not able to compensate the reduced physical time for combustion. Hence, the higher RPM cycles burn typically slower in CAD time. (5) On average, the increased combustion duration in CAD time for higher RPM increases the CAD period, where the spark kernel is highly prone to local turbulence fluctuations. (6) A noted effect of RPM on CCV is the stretched combustion duration in CAD time so that the effect of the initial fluctuations can persist for a longer CAD period. (7) In the present model, the velocity magnitude near the spark largely explains cycle-to-cycle variations in the investigated low RPM range.

1. Introduction

The role of spark-ignited (SI) internal combustion engines (ICE) in marine propulsion and electricity production technology has grown during the past years [1]. In particular, an interest in power-grid stabilization via flexible and distributed small scale solutions has drawn attention to a mature ICE technology. In such applications, start-up time, ramping capability and part load efficiency are critical features, all belonging to strengths of cost-competitive ICE technology [2].

To achieve simultaneously high thermal efficiency and low emission levels, controlled and complete combustion is mandatory in all operating conditions. However, cyclic variation between consecutive combustion events is often present in practical SI engines. Such cycle-to-cycle variations (CCV) are caused by the stochastic nature of internal turbulent flow structures and combustion events [3]. Moreover, use of lean fuel-air mixtures in SI engines, to further reduce emissions during the combustion process, tends to increase CCV [4,5]. This higher CCV is correlated to less intense ignition by spark and low premixed flame speed under lean conditions [4,6,7]. In practice, CCV may become the limiting factor for the operational range of the engine design [8], lead to reduced efficiency due to potential knocking phenomena [9], and enhance unburned hydrocarbon emissions due to incomplete combustion [10,11]. Other practical consequences are undesired power fluctuations (up to ~ 10%) and increase in fuel consumption (up to ~ 6%) [12]. Accordingly, an improved understanding of CCV sources in lean burn SI combustion would be a significant step towards understanding and potentially reducing CCV in engine applications.

Several experimental studies on CCV have been carried out during the past years with focus on e.g. local fuel-air ratio [13,14], and in-cylinder turbulence levels [5,15]. A review by Finney et al. [3] covers

https://doi.org/10.1016/j.apenergy.2019.03.198
Received 20 December 2018; Received in revised form 10 March 2019; Accepted 25 March 2019

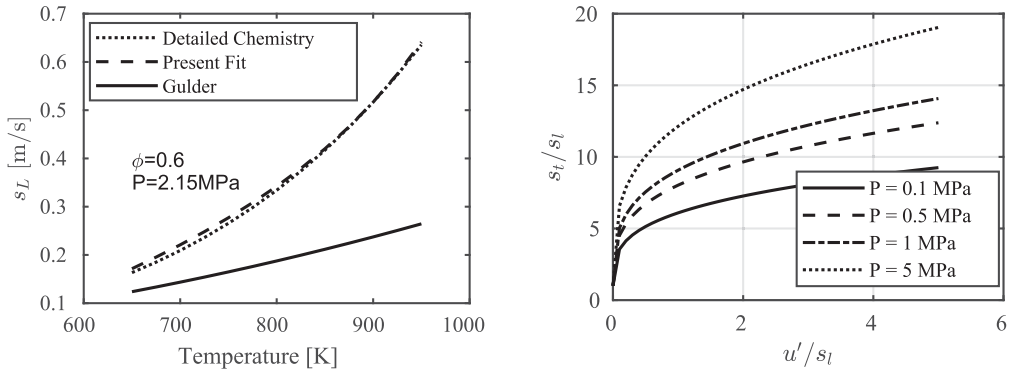

(a) Present s_L correlation performance (b) Muppala turbulent flame speed

Fig. 1. (a) Performance of the developed correlation for s_L compared to Gülder and detailed chemistry (GRI-3.0) at $\phi =$ 0.6 and $P = 2.15$ MPa. (b) s_t/s_L at different pressures based on Muppala correlation [49].

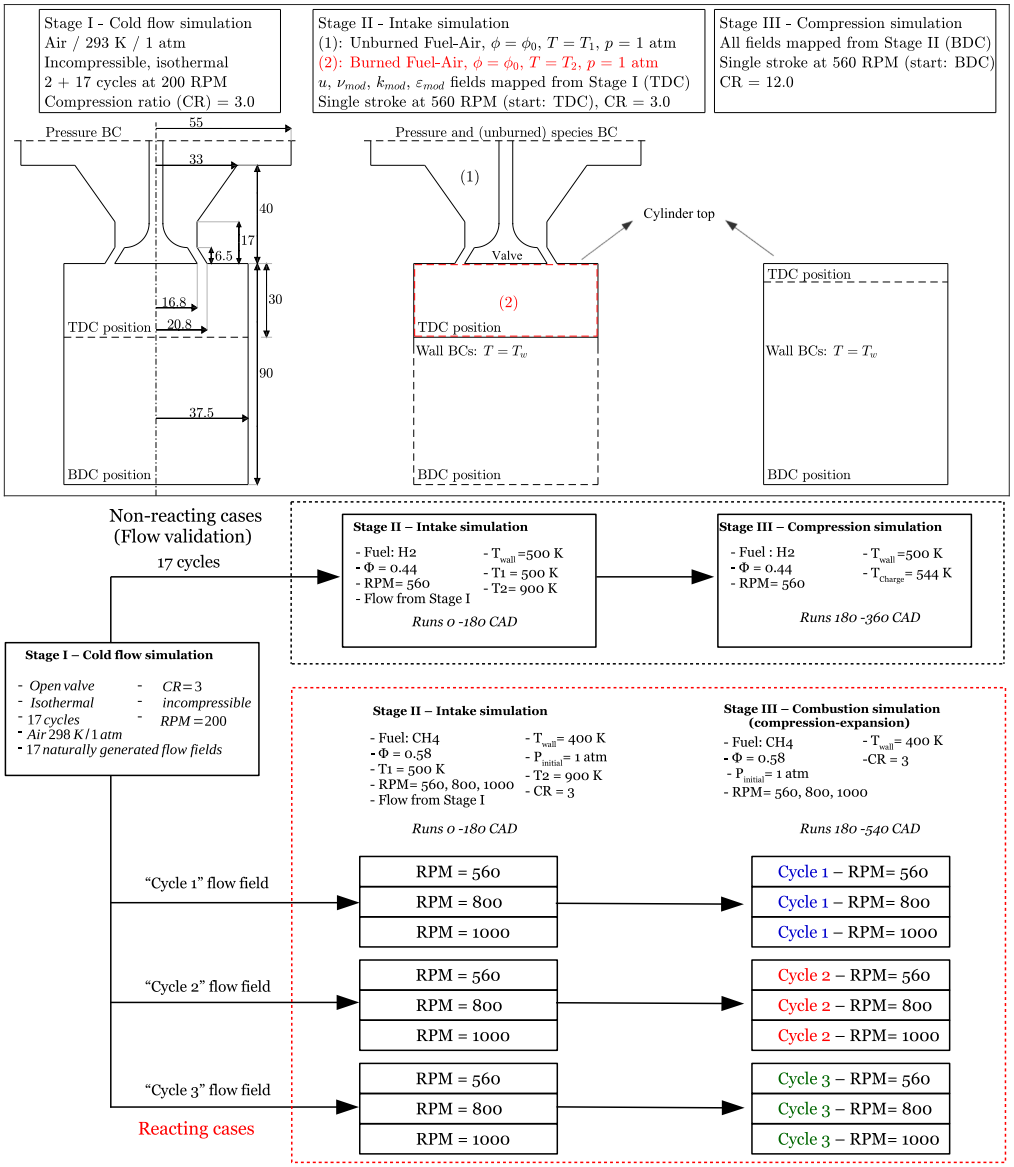

Fig. 2. Description of the non-reacting (according to [31]) and reacting cases: cold flow cycles (Stage I), single intake stroke (II) and compression/combustion cycle (III). System dimensions are expressed in millimeters.

Table 1
Engine and reacting case descriptions (Stage III).

Reacting (stage 3)	Cycle 1	Cycle 2	Cycle 3
RPM [CAD]		560, 800, 1000	
Number of cylinder		1	
Displaced volume [cc]		265	
Stroke [mm]		60	
Squish band [mm]		30	
Bore [mm]		75	
Mesh at BDC [cell count]		2.95×10^6	
Wall temperature [K]		400	
Fuel		CH_4	
Average ϕ		0.58	
Initial pressure [MPa]		0.1	
Compression ratio		12	
Spark time [CAD]		30 BTDC	
Runs [CAD]		360	

the developments in understanding CCV and underlines both stochastic and deterministic effects on cyclic variability in SI engines. Besides experimental works, computational approaches allow quantitative investigation of thermal and flow fields with relevance to physical and chemical processes leading to CCV. In particular, the large-eddy simulation (LES) method allows capturing and identifying unsteady flow phenomena, relevant for the CCV.

A number of LES studies on CCV have been published in recent years, demonstrating the capability of LES to reproduce experimental CCV predictions in certain engine configurations [16–22]. With relevance to this work, several LES investigations have shown the influence of local conditions near the spark on the early flame development and hence, on the whole combustion event (i.e. CCV) [23,21,24,22]. The importance of local conditions near spark have been also indicated by the experimental studies by e.g. Johansson et al. [13], Aleiferis et al. [25] and recently by Liu et al. [26]. However, these experimental and numerical studies have provided only limited insight into the CCV while the relative influence of different global/local factors (spark, air-fuel ratio, thermal and flow field) is still unresolved. Besides, in most LES studies, global measures such as in-cylinder pressure trace is used for validation and only a little attention is paid on e.g. accurate turbulence and wall heat transfer. For reference, the influence of grid resolution has been recently discussed in Refs. [27,28].

The recent CCV LES study by the present authors [24] considered a simplified single-valve engine configuration, for which an extensive direct numerical simulation (DNS) data on flow statistics for a non-reacting engine cycle is available [29–31]. A validation of flow statistics was carried out in Refs. [28,24], yielding good correspondence against the DNS data. After validation, the G-equation level set method, being utilized before in the LES context e.g. in [16,24,22], was utilized to study combustion cycles within the same case configuration. Following

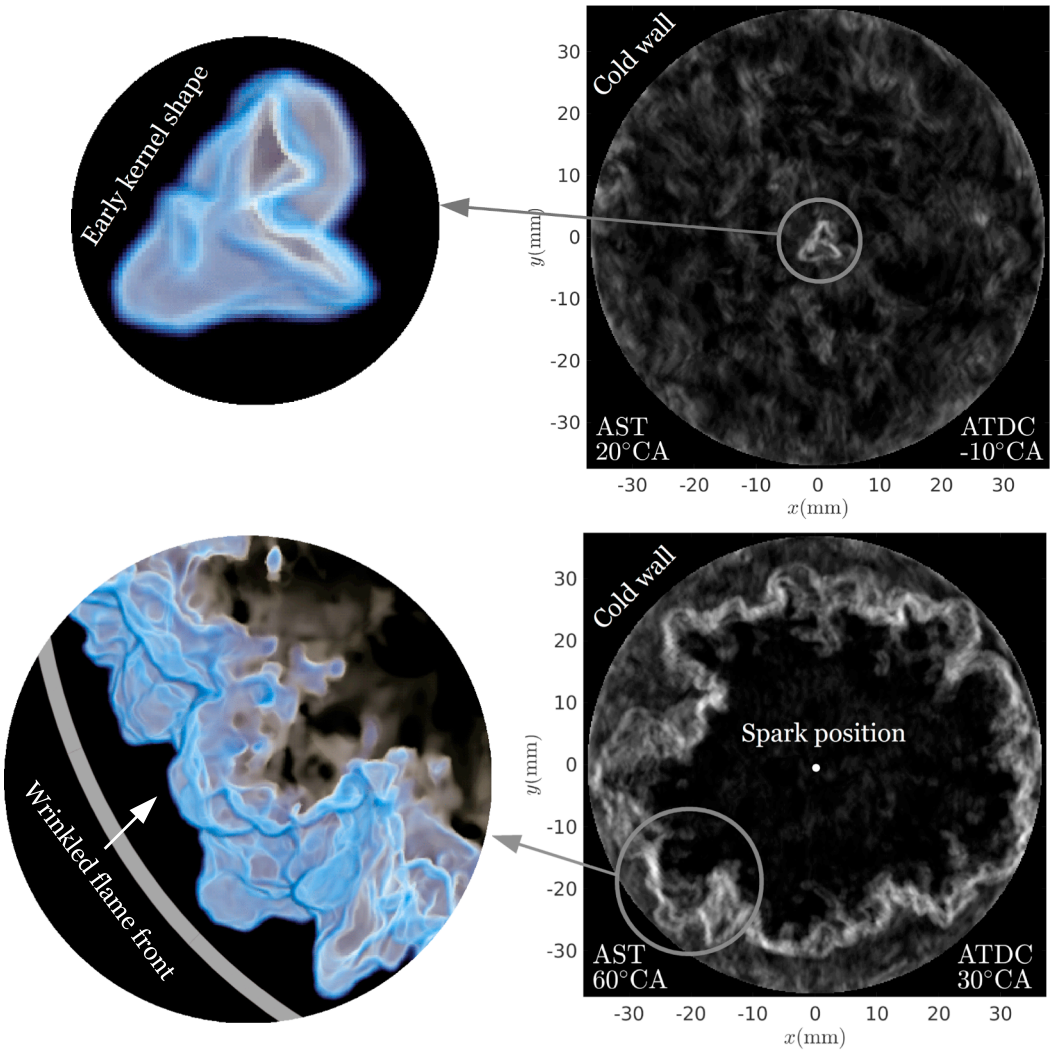

Fig. 3. Numerical Schlieren and zoomed volume rendered flame visualization at an early time of 20 CAD after spark time (top) and a later time at 60 CAD after spark time (bottom).

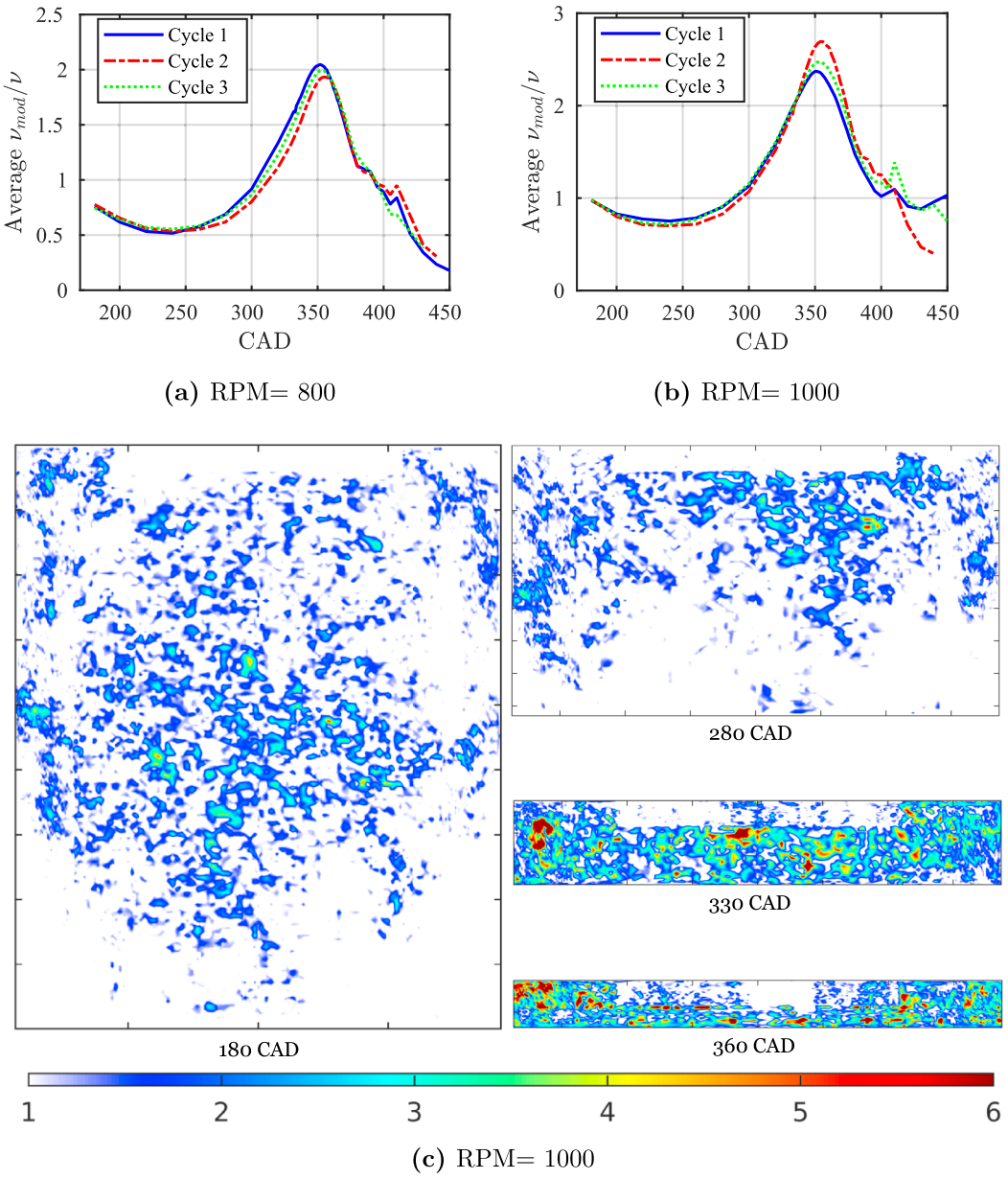

Fig. 4. Average modeled to molecular viscosity ratio (ν_{mod}/ν) for the whole domain at (a) 800 RPM and (b) 1000 RPM. (c) Instantaneous ν_{mob}/ν at 180, 280, 330 and 360 CAD.

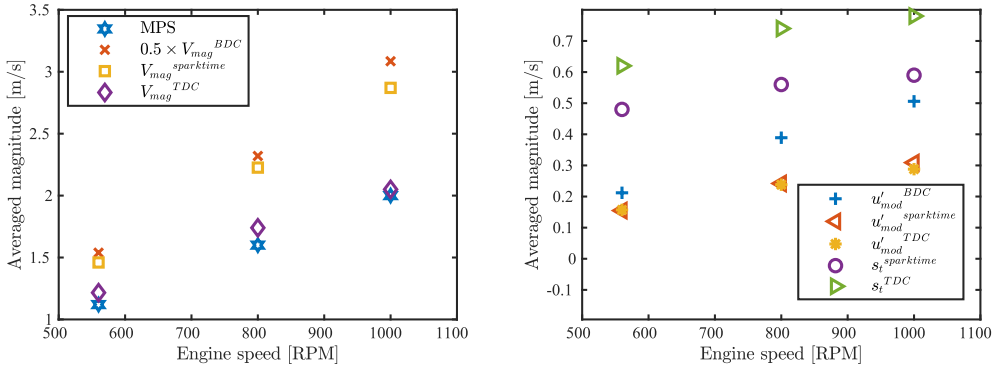

Fig. 5. Engine speed effect on turbulence. The data is averaged over the chosen cycles at each engine speed.

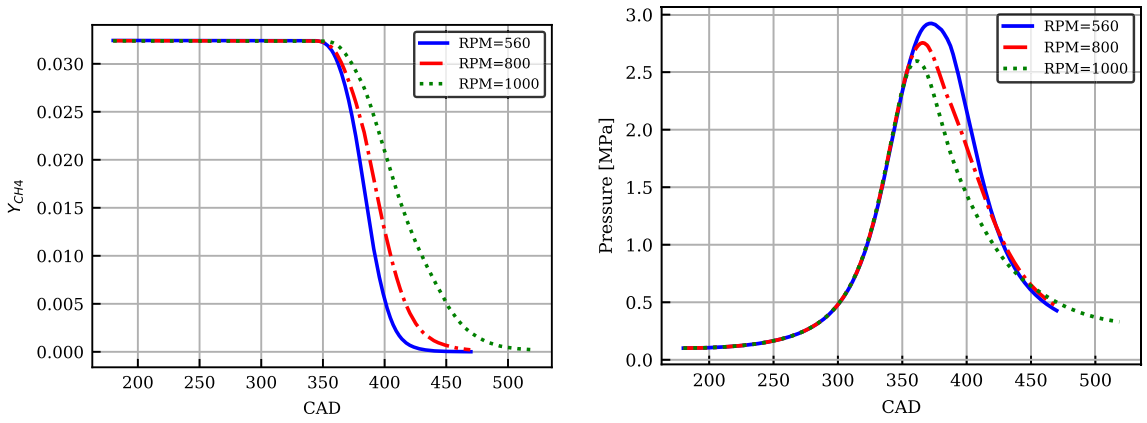

(a) CAD space

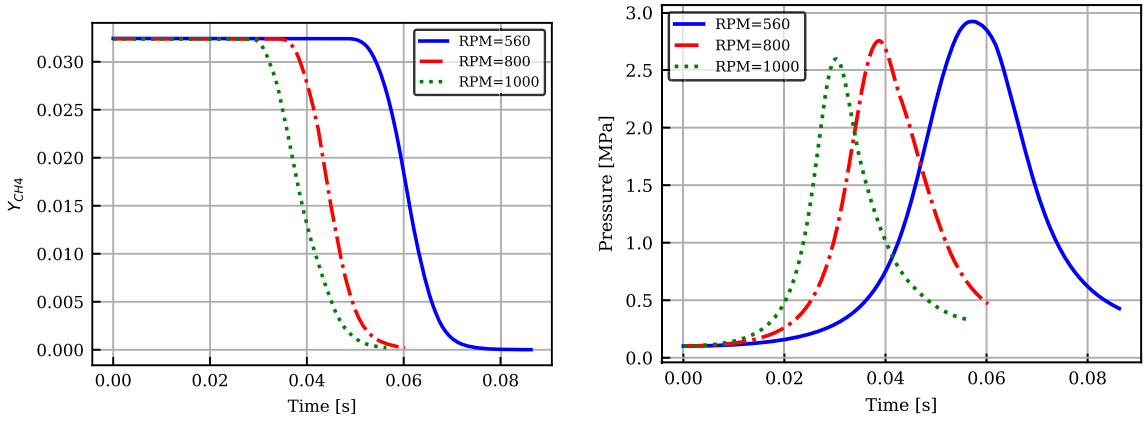

(b) Physical time space

Fig. 6. Comparison of average cycles in terms of fuel mass fraction, and pressure for the three engine speeds. The plots are shown in (a) CAD time, and (b) physical time. In physical time, the time $t = 0$ s corresponds to the spark time to ease comparison of different RPMs.

the previous study of the present authors [24], here we utilize the same scale-resolving LES method, customized near-wall modeling strategy [32,33], and the G-equation approach [34] for a broader range of engine speed (RPM).In our previous study, a rather low 560 RPM engine speed was investigated, while in the present study the LES analysis is extended to cover higher 800 and 1000 RPM values. Such RPM values are relevant for engines in marine and electricity generation sectors.

Only a few studies, whether numerical or experimental, have specifically commented on engine speed effects on CCV origins in SI context [14,35–37], and they have reported rather diverse conclusions on the effects of RPM on CCV. Such contradictory conclusions can be related to two competing effects of RPM increase in completion of combustion as discussed by Sen et al. [38]. First, higher turbulence intensity leads to higher flame speed which supports the whole charge combustion, and second, due to higher rotational speed, less time is available for flame propagation to complete the combustion. Such opposite effects influence the early flame development and the time period that ignition kernel is still prone to any perturbations in the system [38].

In a review paper by Young et al. [35], it was reported that increasing engine speed usually leads to an increased cyclic combustion variation. It was suggested that an increase in flame speed might have a significant effect on such cyclic variations. Also, more recently, Reyes et al. [14] studied the engine speed effect on cyclic combustion variations. The analysis was carried out at 1000, 1750 and 2500 RPM, and indicated that there is a strong positive correlation on engine speed and CCV.

In contrast to the above observations, experiments carried out by Aydin et al. [36] showed that an increase in engine speed resulted in lower total combustion duration and CCV. The result was considered as a combined effect of higher turbulence kinetic energy, improved mixture state, and higher flame speed. Moreover, Huang et al. [37] studied CCV in a spark ignition engine fueled with natural-gas/hydrogen blends combined with exhaust gas recirculation (EGR). The higher engine speed test indicated lower cyclic variations due to enhanced turbulence and swirl within the cylinder. Such diverse findings regarding engine speed correlation with CCV motivate detailed numerical studies such as this study.

Based on the provided literature survey, we note the following research gaps: (1) Only a few CCV studies have focused on engine speed effects on cyclic combustion variations, (2) majority of the RPM-based CCV studies solely reported the global CCV trends without a linkage to the details of in-cylinder combustion phenomena, (3) the previous RPM CCV studies provided diverse conclusions regarding engine speed effects on CCV origins, and (4) the conclusions by Ghaderi Masouleh et al. [24] on combustion CCV have not been extended for higher RPM values. In particular, the leading hypotheses for the present work stem from our previous work, where it was noted that 1) combustion CCV is dictated by early conditions around flame kernel after spark timing and 2) early combustion rate is mostly dictated by turbulence level, while thermodynamic effects are secondary.

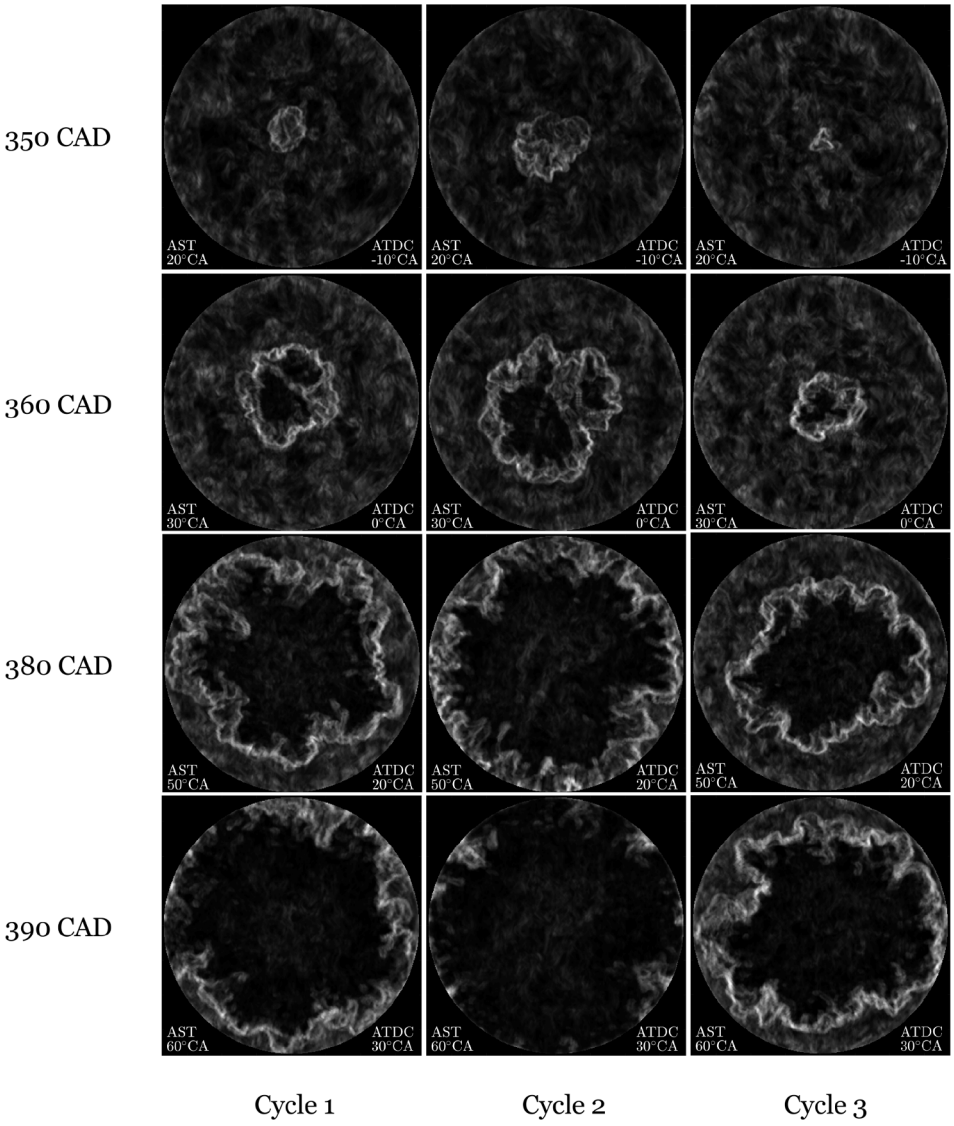

Fig. 7. Numerical Schlieren visualization of flame propagation for cycles 1–3 at 560 RPM. It is noted that the faster a cycle starts burning, the faster it continues to burn.

The present study is limited to 560–1000 RPM range for two reasons. Such low RPMs have relevance to marine engines and enable us to maintain flow characteristics close to the non-reacting validation conditions at 560 RPM [30,24]. Considering the observed research gaps in this context, main objectives of the present study are to: (1) extend the authors' previous study [24] by exploring higher engine speed cases, (2) quantify the effect of engine RPM on turbulence and CCV in the studied cases, (3) investigate the role of initial conditions on the observed CCV, (4) compare effects of thermal and flow fields on cyclic variations as engine speed is modified.

2. Methods

2.1. Fluid dynamical approach

The methodology in this work is the same as that described in our previous study [24]. In the following, a summary of the used models is provided. The present work utilizes a zonal hybrid LES/RANS methodology with wall treatment (HLR-WT) [33,24]. While LES accounts for the core flow using an explicit SGS model (σ-model [39]), a low-Reynolds number RANS model ($k-\epsilon$) is employed in the near-wall regions. More details regarding the continuity of the modeled turbulent viscosity between the core and wall regions are provided in [33,24].Besides, for the wall treatment, a one-dimensional wall model, developed by Nuutinen et al. [32] for engine-like boundary layers in the RANS context, is implemented in wall-normal direction under a thin boundary layer assumption. Further details regarding the implementation of this model can be found in [33].

2.2. Combustion model

The utilized combustion model is the same as that in our previous study [24]. The combustion model is the so-called G-equation, proposed by Williams [34], which describes flame front evolution based on the level-set method. This model is used in different engine-relevant LES works, e.g., [40,16,19,41]. Pitsch and Duchamp de Lageneste [42] formulated G-equation in the LES context as

$$\bar{\rho}\frac{\partial \widetilde{G}}{\partial t} + \bar{\rho}\widetilde{u}\cdot\nabla\widetilde{G} = \bar{\rho}s_t\ |\nabla\widetilde{G}|, \tag{1}$$

where t, ρ, u, s_t, -, and $\sim$ denote time, density, velocity vector in unburnt mixture, turbulent flame speed, spatial filtering and spatial Favre filtering, respectively.

In G-equation, s_t is typically found based on an empirical

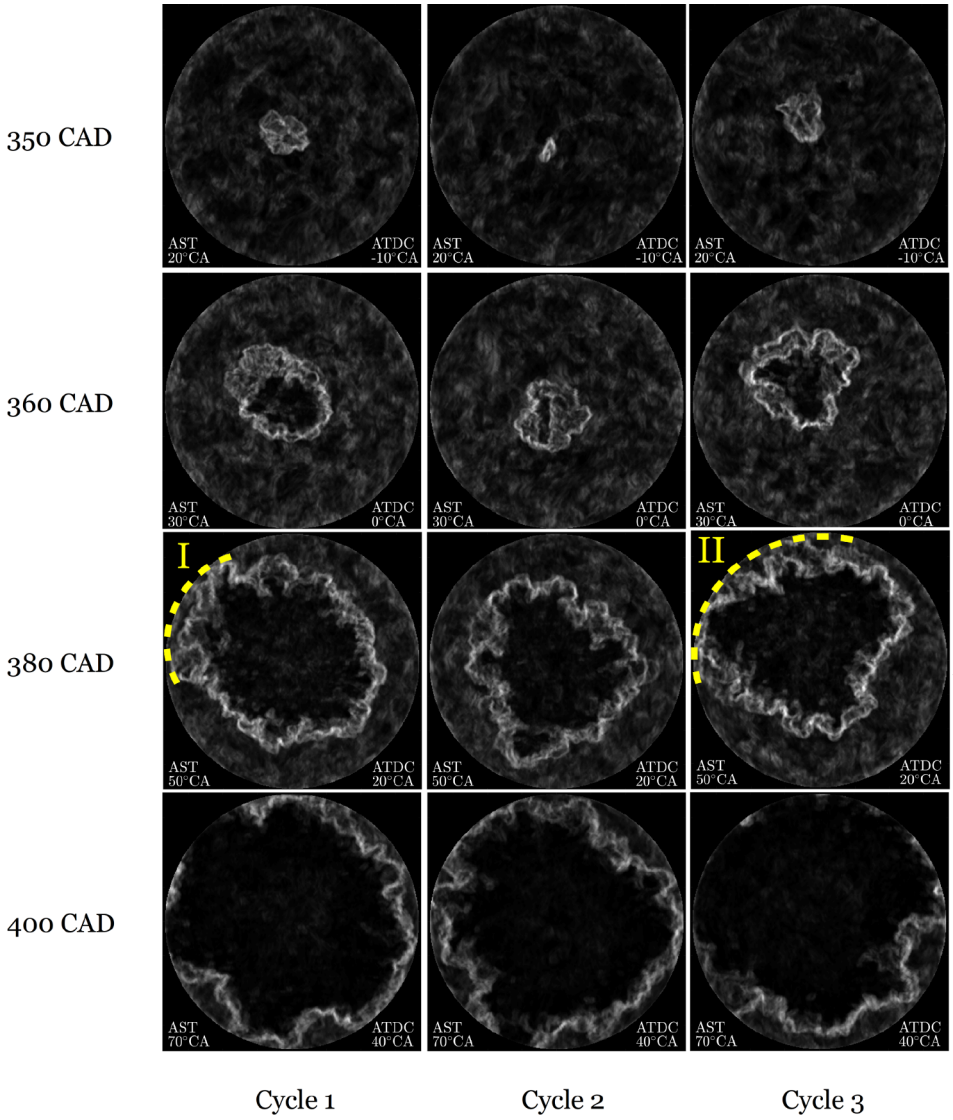

Fig. 8. Numerical Schlieren visualization of flame propagation for cycles 1–3 at 800 RPM. The flame area growth around regions (I) and (II) slows down after flame reaching the walls.

correlation. There are variety of empirical correlations suggested for s_t, e.g. [43–48]. With relevance to this work, it is desired to utilize an empirical correlation that is validated at higher than atmospheric pressures. Among different available correlations, Muppala correlation, [49], has been shown to better predict s_t up to 0.3 MPa in different applications [49–51]. In this regard, similar to [24], Muppala correlation has been used,

$$s_t = s_L + s_L \frac{0.46}{Le} Re_t^{0.25} \left(\frac{u'_{mod}}{s_L}\right)^{0.3} \left(\frac{P}{P_0}\right)^{0.2}, \quad (2)$$

in which Re_t, u'_{mod}, s_L, Le and P_0 are turbulent Reynolds number, the modeled velocity fluctuation, laminar flame speed, Lewis number ($Le = 1$) and reference pressure ($P_0 = 0.1$ MPa), respectively. More details of s_t implementation in LES/G-equation context is available in our recent work [24].

In LES/G-equation context, s_L is commonly predicted using an empirical correlation as a function of composition and thermodynamic state of the mixture, see e.g. [52]. These correlations, however, are not validated at engine-like conditions due to the lack of experimental studies on laminar flames at those conditions. Although there have been some efforts to improve these correlations for methane fuel at engine-like conditions, such as [53,54], they do not cover the entire conditions in the present work. As such, the correlation developed and examined against available correlations for s_L in our previous study, [24], has been utilized here. As features and defects of this correlation have been extensively discussed in [24], here, it is only briefly introduced.

The s_L correlation is developed using detailed chemical kinetics simulations in one-dimensional laminar configurations, where open-source chemical kinetics library Cantera [55] is used. The laminar free-flame problem is solved using the GRI-3.0 methane mechanism [56] at conditions spanned by $T = 400$–950 K, $P = 1$–50 bar and $\phi = 0.45$–1.1. It is worth mentioning that the choice of chemical kinetics could have a considerable impact on the laminar flame speed solutions [57]. GRI-3.0 has been extensively validated at different conditions as a representative of methane fuel [56]. Therefore, the mechanism was chosen for the present study. More details on the s_L correlation function can be found in [24]. Fig. 1(a) represents a comparison between detailed chemistry solutions, the employed fit-function [24] and Gülder empirical correlation [52], indicating that chemical kinetics predict substantially higher laminar flame speed than the Gülder correlation.

Fig. 1(b) illustrates the representation of s_t/s_L by Muppala correlation. The expected relationship between s_t/s_L and u'/s_L has been shown in Peters [58] through a meta-analysis of experimental data from Abdel-Gayed and Bradley [59], revealing that s_t/s_L increases linearly for

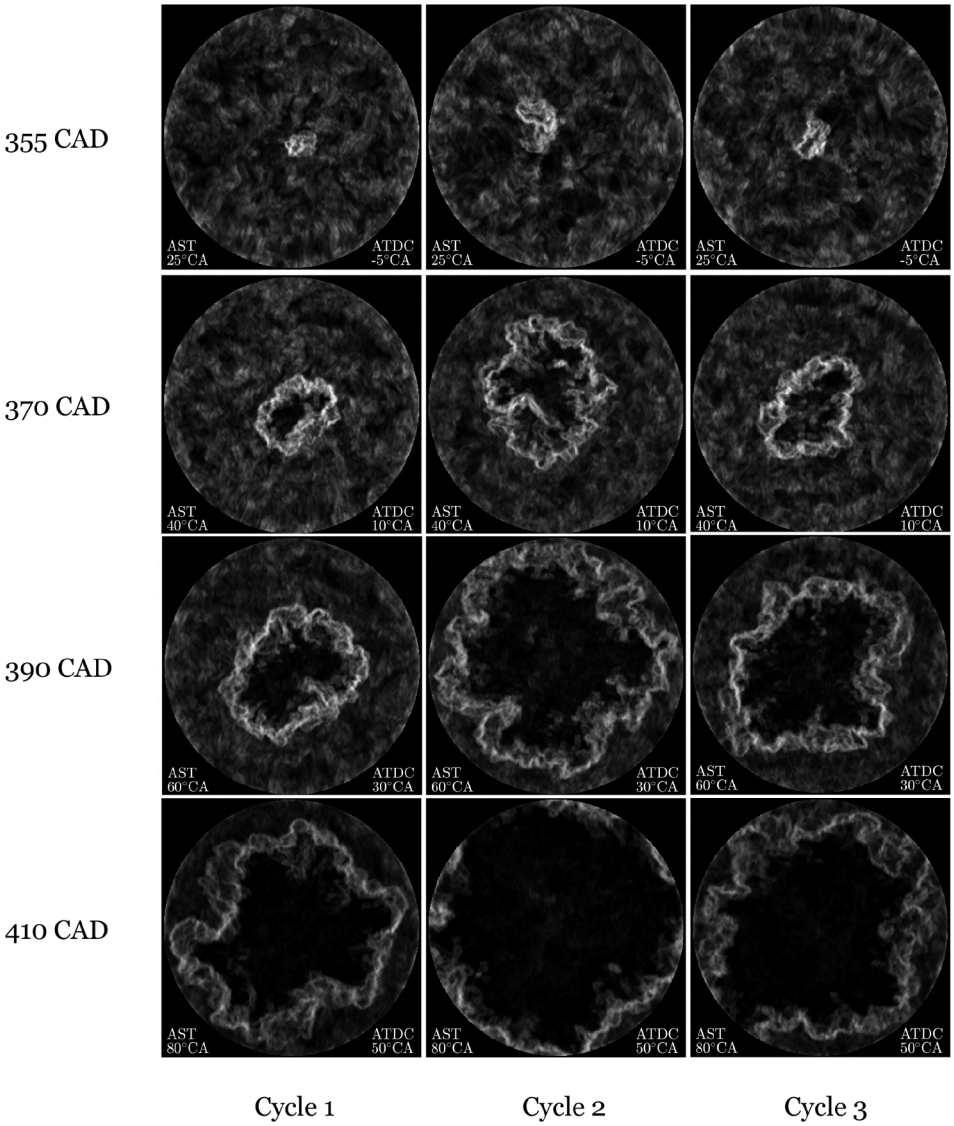

Fig. 9. Numerical Schlieren visualization of flame propagation for cycles 1–3 at 1000 RPM. The faster a cycle starts burning, the faster it continues to burn.

low turbulence intensities. As u'/s_L continues to increase, a bending slope effect is observed until eventually the s_t/s_L is insensitive to the increasing u'/s_L. The Muppala correlation in Fig. 1(b) follows the expected trend, while it is found in a priori studies [60–62] that many of the existing models tend to over-predict s_t/s_L.

It is noteworthy that in the G-equation it is assumed that the combustion source term propagates the flame with turbulent flame speed which further depends on the laminar flame speed (see Eq. (2)). The contribution of SGS velocity is seen by the combustion model via the s_t-correlation only. According to Eq. (2), s_t depends weakly on u'_{mod}. Also, the flame and the reaction zones are assumed to be thin. The low RPM range in the present study is considered to be consistent with these assumptions.

2.3. Ignition treatment

An ignition treatment similar to that in [24] is utilized here. A spherical flame kernel with a predefined diameter of 0.2 mm is initialized with an enthalpy source term at the ignition time. The G-equation level set model uses the source term to determine the zero-level set, i.e. the flame position. In particular, after spark initialization, the G field undergoes a pre-processing step to enforce the condition that the function G is a signed distance function. Similar ignition treatments are used in [63,16,19]. Transition from laminar to turbulent flame speed is ignored and from the ignition time onwards, the flame propagates with turbulent flame speed [16]. Fontana and Galloni [64] have indicated that spark timing is highly relevant in SI engine combustion control. In order to isolate the engine speed impact from any other effects, the spark timing is kept constant at 330 CAD for all the engine speeds, i.e. 30 CAD before top dead center (TDC).

2.4. Geometry and charge preparation

The computational set-up is based on the three-stage process described in our previous work [24]. The process produces relevant initial charges for reacting cases considered in this study, as illustrated in Fig. 2. These three stages are summarized in the following. Stage I is an isothermal incompressible flow case following the experimental study by Morse et al. [65]. This stage runs for 17 cycles and generates 17 flow fields to be used in following stages. In Stage II, a single flow field from Stage I is taken, while uniform fuel composition and temperature are set in the intake channel part (Fig. 2, marker (1)). Moreover, a burnt mixture of air and residual gases at $T = 900$ K is set in the initial field below the valve level (see Fig. 2, marker (2)). Finally, Stage III starts by closing the valve at 180 CAD, i.e. bottom dead center (BDC), after which the mixture is compressed, ignited at 330 CAD, and then,

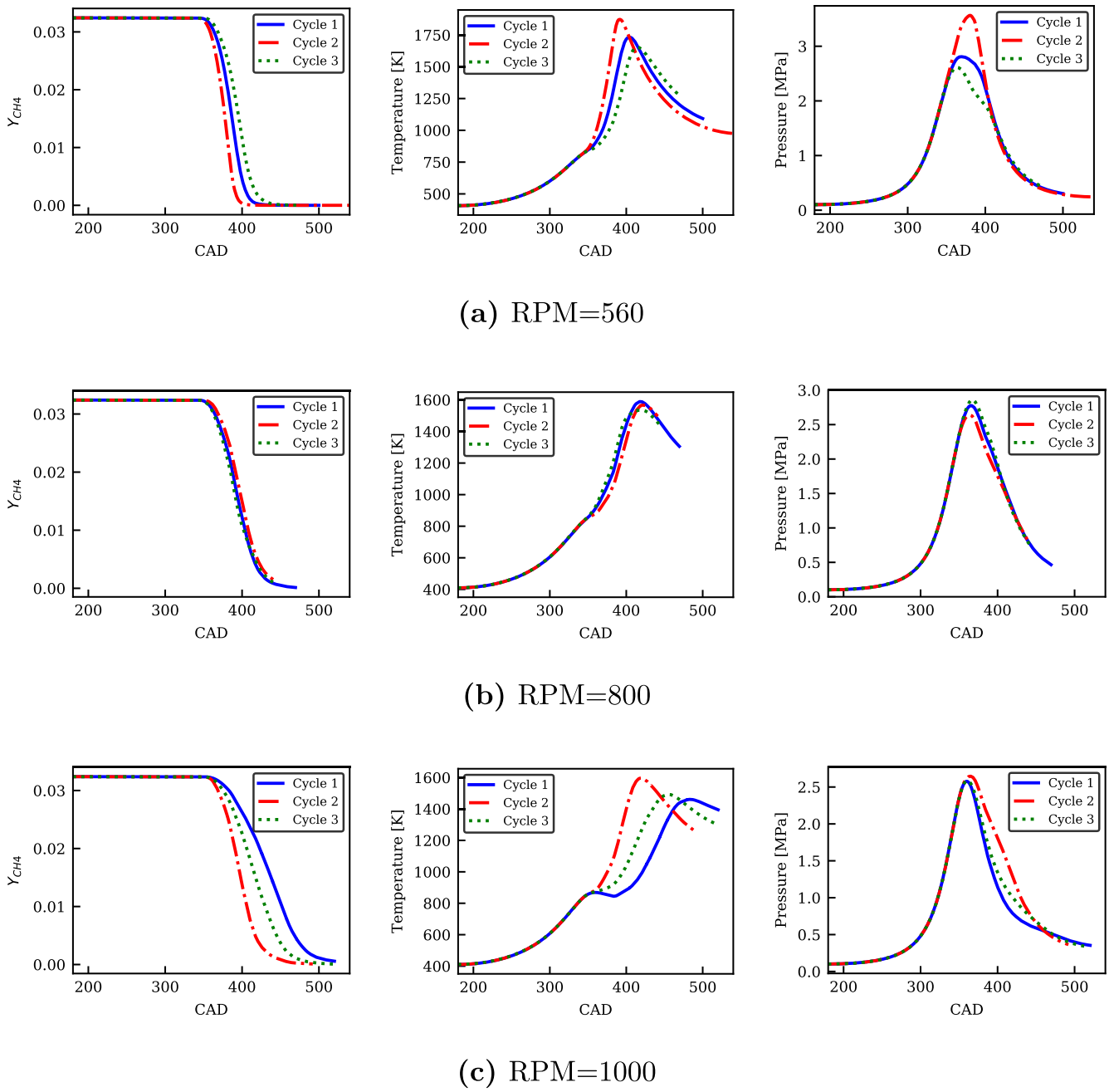

Fig. 10. The density-weighted mean cylinder CH_4 mass fraction, average temperature and pressure of the three studied cycles at (a) 560 RPM, (b) 800 RPM, and (c) 1000 RPM. The CCVs, including the noted low CCV at 800 RPM, are further analyzed in the following sections.

expanded.

The present configuration has been validated in our recent work [24] at non-reacting conditions against DNS data [29–31] regarding the phase-averaged mean axial velocity, RMS velocity profiles, total heat flux, temperature probability density functions (PDF), and instantaneous cylinder head heat flux distribution. For brevity, we do not show those validations here. Also, similar to our recent work [24], in order to provide a more interesting case regarding cyclic variations in reacting cases, certain parameters such as equivalence ratio, fuel and wall temperature have been modified compared to DNS studies. Thus, similar settings have been employed for the present study as well.

Table 1 describes geometry specifications and characteristics of the studied cases at stage III. Calculation of piston position in this engine-like geometry is based on a sinusoidal function according to [29–31]. In addition, Fig. 3 shows a numerical Schlieren image with a zoomed volume rendered visualization of the flame front. The figure introduces the computational setup including the spark position and the location of the cold walls in the studied engine geometry. It also visualizes the asymmetric early shape of kernel. The shape of kernel is modified by the local flow field close to the spark location. The kernel asymmetry grows in time and leads to the observed very corrugated flame front close to the end of combustion.

2.5. Mesh

In our recent study [24], a computational mesh with an identical core and near-wall resolution was utilized and validated against DNS data at non-reacting conditions for low RPM cases (560 RPM). This mesh has been utilized in the present study and its main characteristics are summarized in the following. The mesh resolution is 0.6 mm, while

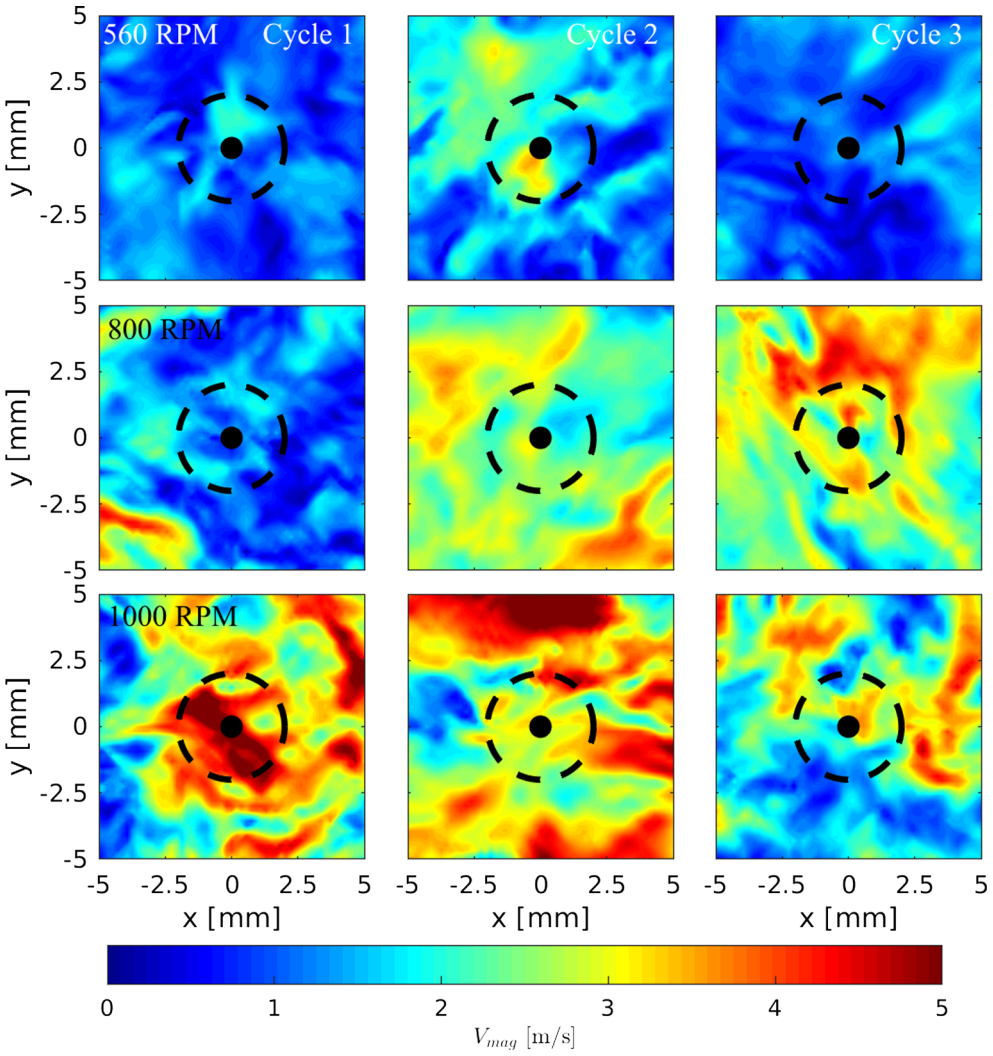

Fig. 11. A zoomed view on instantaneous V_{mag} field at the spark plane (wall distance of 1.0 mm) at t_{spark} = 330 CAD. The dashed line denotes a 2 mm radial volume used in the analysis of Fig. 12(b). Rows and columns correspond to an increasing RPM and cycle number, respectively.

the probability distribution functions (PDF) of temperature and velocity show weak sensitivity to changes of the core resolution from 0.7 to 0.4 mm (see [24]). The cell layers are removed/added during the compression/expansion to maintain the core resolution relatively constant. The mesh includes a cylindrical refinement region at the cylinder head, with a height of 4 mm and diameter of 44 mm, to better capture the flow and thermal fields near the spark region. In the refinement region, the grid size is the smallest close to the top of the cylinder (0.05 mm) and it gradually increases towards the bottom of the refinement region (cell size 0.25 mm) (see supporting figures in [24]).

Here, turbulent to molecular viscosity ratio (ν_{mod}/ν) has been employed as an indicator of the local mesh quality in a similar fashion as in [28,66]. Fig. 4(a) and (b) demonstrate $\langle \nu_{mod}/\nu \rangle$ for the whole domain for 800 and 1000 RPM, respectively. Fig. 4(a) and (b) indicate that the $\langle \nu_{mod}/\nu \rangle$ is increased with the increased engine speed as expected. The $\langle \nu_{mod}/\nu \rangle$ represents peak values of ≈ 2 and 2.8 on average for the 800 and 1000 RPM cases, respectively. The peak values are obtained at TDC, where the rate of dissipation increases.

At 1000 RPM, in particular, cycle 2 represents the highest local ν_{mod}/ν value. Fig. 4(c) shows the instantaneous ν_{mod}/ν for cycle 2 at 1000 RPM at 180, 280, 330 and 360 CAD to provide a better understanding of mesh performance in this case. Although the local ν_{mod}/ν ratio reaches the value of ≈13 at small local spots at TDC (at 360 CAD), it is observed that the ratio mostly remains smaller than 5, highlighting a reasonably good LES quality [67]. It is worth noting that in more demanding LES scenarios, such as the study by Nguyen et al. [68], larger values of such ratio (exceeding 20) have been reported.

3. Results

3.1. Engine speed effect on global turbulence and combustion process

The link between engine speed and flow velocities is established in Fig. 5. The figure shows both average resolved velocity (V_{mag}) and modeled velocity (u'_{mod}) magnitudes at BDC, TDC and spark timing (t_{spark}). Additionally, turbulent flame speed (s_t) at BDC and spark timing (t_{spark}) are reported. As expected, the increase of engine speed not only indicates higher mean piston speed (MPS), but also higher turbulence levels and flame speeds. In particular, average V_{mag} and engine speed correlate strongly at the three time instances. Also, u'_{mod} and s_t increase with RPM, but on a different scale. While u'_{mod} depends relatively strongly on RPM, its overall effect is manifested via s_t. As can be seen, s_t changes only about 20% in the investigated RPM range and thus the average s_t can be considered to be almost constant. Next, in order to provide a better understanding on combustion rate at different engine speeds, the average fuel consumption rate and in-cylinder pressure are considered.

Fig. 6 displays fuel mass fraction and in-cylinder pressure, averaged

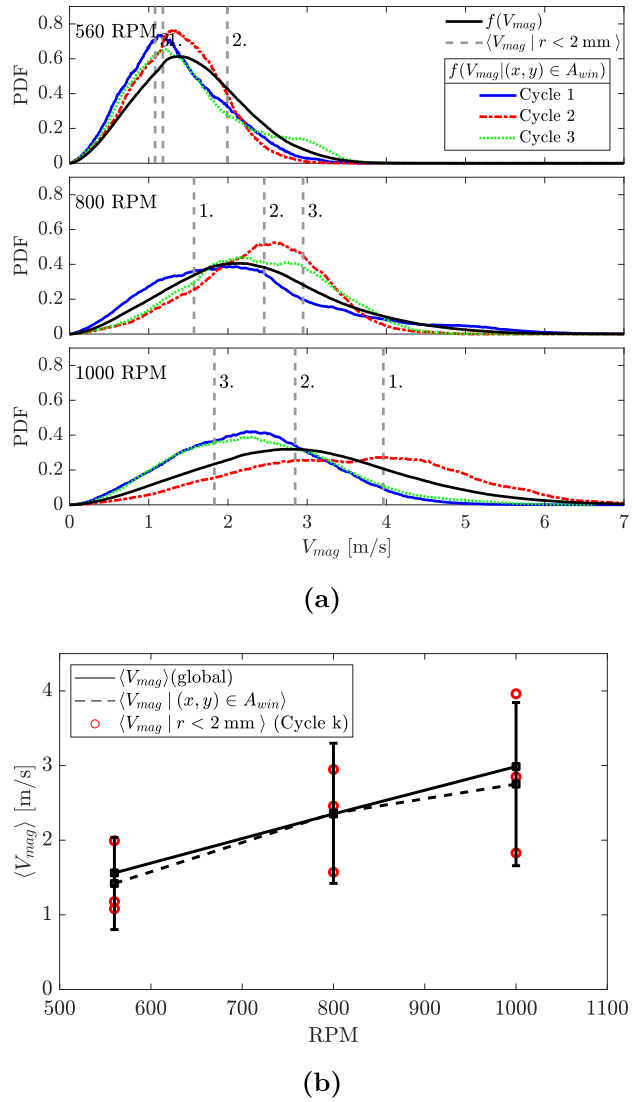

Fig. 12. Global and local V_{mag} statistics at $t = t_{spark}$, i.e. at 330 CAD. (a) Black solid line is a global PDF from the whole domain, while the cycle PDFs correspond to local PDFs evaluated in the near spark window A_{win} of size 10 by 10 mm. The dashed vertical lines correspond to even more local averages calculated within 2 mm radius from spark. (b) The mean values corresponding to PDFs as a function of RPM. The error bars denote the averaged standard deviation over all cycles within A_{win}.

over the three cycles, at each engine speed in (a) CAD space, and (b) physical time space. It is observed that on average, higher engine speed indicates an expected fast combustion in physical time, while contrastingly, higher RPM burns slower in CAD space. These opposite trends in the two spaces are correlated with the reduced physical time for combustion at higher engine speeds (42% at 800 RPM and 78% at 1000 RPM, respectively).

According to Fig. 6, at higher RPMs, despite the increased turbulence and flame speed, a longer combustion duration in CAD space is observed. This implies that, in the present conditions, turbulence and flame speed increase at higher RPM values does not compensate the decreased time for flame propagation. It is noteworthy that here t_{spark}= 30 CAD BTDC in all cases in order to isolate engine speed effects from any other possible changes in case setup. Considering the noted differences in average burning rates at different engine speeds, in the following sections, effects of engine speed on CCVs are investigated and discussed.

3.2. Observations of cycle-to-cycle variations at different engine speeds

Figs. 7–9 provide a qualitative comparison on temporal flame evolution by numerical Schlieren images at the three chosen cycles at 560, 800, and 1000 RPM, respectively. The visualization is generated based on the line-of-sight view of integrated log ($\gamma + |\nabla\rho|$), where γ is a small, positive constant. It was previously reported by Ghaderi Masouleh et al. [24] that local turbulence and thermal fluctuations around the ignition kernel at early time instances after spark timing (AST) can cause significant changes to the kernel development and flame propagation at 560 RPM. It was also discussed that global combustion rate of a cycle is strongly dependent on the initial kernel development; i.e. there is a trend that initially quicker kernel development results in faster combustion progress throughout the cycle.

Figs. 7–9 indicate early signs of CCV already during the first 10 CADs AST. This implies that combustion CCV and initial conditions may be closely coupled. At 560 RPM, Fig. 7 indicates how initial discrepancies between the cycles sustain from 350 to 390 CAD. At 800 RPM, Fig. 8 indicates that the kernel in cycle 2 is the least developed at 350 CAD. However, at later times, cycle 2 reaches cycles 1 and 3. Qualitatively, a potential cause for such an effect could be the reduced combustion rate of cycles 1 and 3 as the flame fronts reach the cylinder walls and the flame area starts to be reduced. Such points are denoted by I and II in Fig. 8. As a remark, we note that modeling flame-wall interaction is a highly challenging topic and that neither the present combustion or wall-models are tailored to account for such reacting flow-heat transfer phenomena.

Finally, at 1000 RPM, in Fig. 9, significant discrepancies between the cycles are noted. Cycle 2 represents the most developed kernel at 355 CAD. Similar to our observations at 560 RPM, flame propagation in cycle 2 (the most developed kernel) remains the fastest throughout the combustion cycle. Next, we shift the focus towards more quantitative analysis of the results.

In order to quantify the noted qualitative observations on cycle-to-cycle variations, Fig. 10 depicts density-weighted averages of fuel mass fraction, in-cylinder temperature and pressure for the three cycles for the three engine speeds. Considering Fig. 10(a) at 560 RPM, consistent with the numerical Schlieren in Fig. 7, cycles 2 and 3 feature the fastest and the slowest consumption rates of fuel, respectively. The clear differences in fuel consumption are noted to arise before 340 CAD (10 CAD AST). It is noted that, despite the simple geometry in the present set-up, relatively large discrepancies in peak pressures, $\Delta_{PP} \approx 30 - 35$ %, are observed at 560 RPM.

Considering Fig. 10(b), different cycles at 800 RPM indicate only slight differences in pressure, temperature, and fuel burning rate. At 800 RPM, in contrast to 560 RPM cases, the modest initial differences between the cycles remained small, $\Delta_{PP} \approx 7 - 9\%$, throughout the combustion process. Moreover, Fig. 10(c) demonstrates that at 1000 RPM, the initial differences between the cycles are firstly larger than at the other RPM cases. Secondly, these differences sustain and also increase for a relatively long CAD period. Such an increase is understandable due to the prolonged average combustion duration of high RPM cases in CAD time.

As a remark, we carried out an additional sensitivity test on spark position effects for Cycle 2 at 800 RPM by shifting initial spark position in two different locations on the same spark plane within ≈ 1 mm from the original spark position (not shown herein for brevity). The additional check indicated that the combustion rate of Cycle 2 was not sensitive to such relatively small changes of spark position. However, more detailed investigations on spark position effects were considered to be outside the scope of present paper and thereby, this matter was not further investigated herein.

3.3. Global and local velocity distributions

Next, to understand the cyclic variation in each case with a varying

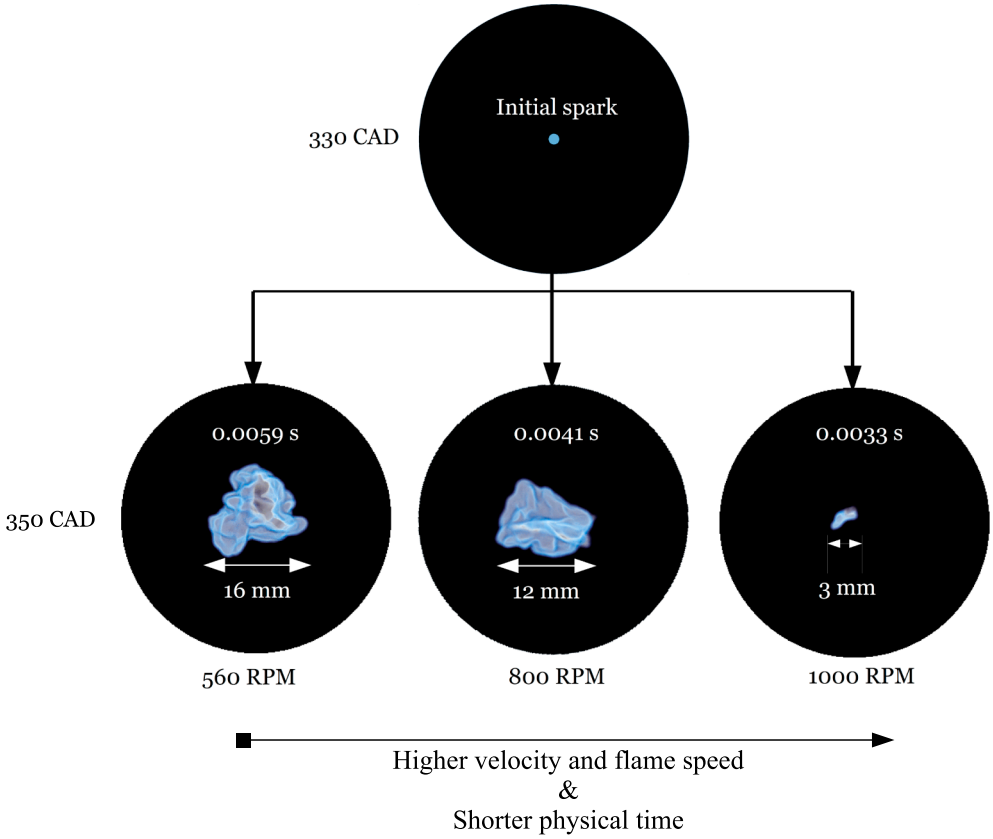

Fig. 13. Instantaneous flame front at 350 CAD for cycle 1 at 560, 800 and 1000 RPM. Increasing engine speed reduces the early and average burning rate of the cycle in CAD space.

RPM, global and local analysis of the velocity distribution is considered. As shown in our previous work at 560 RPM [24], the cycle-to-cycle variation of global PDFs of resolved velocity magnitude and temperature from the unburnt region was noted to be minimal. Similarly, at 800 and 1000 RPM, global statistical similarity for V_{mag} PDFs is observed and provided in Appendix B.

The observations of high cyclic variation around the spark position at early times in Figs. 7–9 is consistent with our leading hypothesis that, for different RPMs, the initial conditions may be essential, and that such variations could potentially impact the global combustion rate of a cycle. Next, the statistical fluctuation of velocity between the cycles and the three RPMs is analyzed in terms of two PDFs: (1) the global PDF of V_{mag}, estimated from the entire cylinder volume at spark time, and (2) the local PDF of V_{mag}, calculated in the vicinity of the spark at t_{spark}.

Fig. 11 illustrates the instantaneous V_{mag} fields at the spark plane (wall distance ≈1.02 mm) at t_{spark} for all cases. As expected, the overall V_{mag} values increase with increasing RPM. Within the immediate vicinity of the spark, clear variations in velocity field between the cycles can be observed. However, it is worth noting that by inspecting such a planar data slice, direct correlations on the corresponding combustion rate should not be considered.

In order to analyze the V_{mag} statistics near spark region at $t = t_{spark}$, Fig. 12a represents the global and local V_{mag} PDFs. The local domain A_{win} is defined as the 10 mm × 10 mm window, represented in Fig. 11. It should be noted that PDFs consider all cells on A_{win} and in volume, i.e. in the third direction. In addition, the mean V_{mag} value inside a 2 mm radius from spark is presented by vertical dashed lines. Fig. 12a shows that the local PDFs and near spark mean values may deviate from the global averages considerably, depending on the cycle.

Fig. 12b shows a monotonic growth of globally and locally estimated mean V_{mag} value ($\langle V_{mag} \rangle$) as a function of RPM at $t = t_{spark}$. Such a trend is consistent with Fig. 5 on V_{mag} increasing with RPM due to increased MPS. It is noted that not only does V_{mag} increase but also the standard deviation increases with RPM, both globally and locally. However, considering individual cycles, it is noted that the actual V_{mag} at the spark position at t_{spark} can vary substantially from cycle-to-cycle. We note that the mean piston speed normalized $\langle V_{mag} \rangle$ mean and standard deviation values are close to each other, within 15% and 7%, respectively.

Several previous works have noted the role of flow initial conditions near the spark on determining the level of CCV [23,21,24,22]. However, comparison of Figs. 12 and 10 shows that correlation between the CCV and local V_{mag} distribution shapes and near spark mean values at the spark timing (t_{spark} = 330 CAD) does not necessarily apply in every case. For example, in the 800 RPM cycles, the mean $\langle V_{mag} \rangle$ show equivalent variation compared to the 560 RPM, whereas in contrast, only mild cyclic variation in combustion rates is noted.

As the flows are 3d and transient, we next consider time-dependent statistics at $t > t_{spark}$ in order to provide a more profound view on possible sources of cyclic variation. As a remark, several previous non-reacting studies [28,30,31,69] have reported the high relevance of the intake phase and the associated flow structures on turbulence CCV. In general, such history effects contribute to the build-up of the presented statistics.

3.4. Flame front evolution

As noted earlier in Fig. 6, higher RPM cases burn slower in CAD space on average. Consistently, Fig. 13 illustrates that the flame kernel initially grows the fastest for 560 RPM and the slowest for 1000 RPM. On average, increasing RPM increases the CAD period, when the flame kernel surface area is small and expected to be highly prone to fluctuations in local flow. However, it is important to note that the initial conditions may further cause CCVs, which can break the average cycle

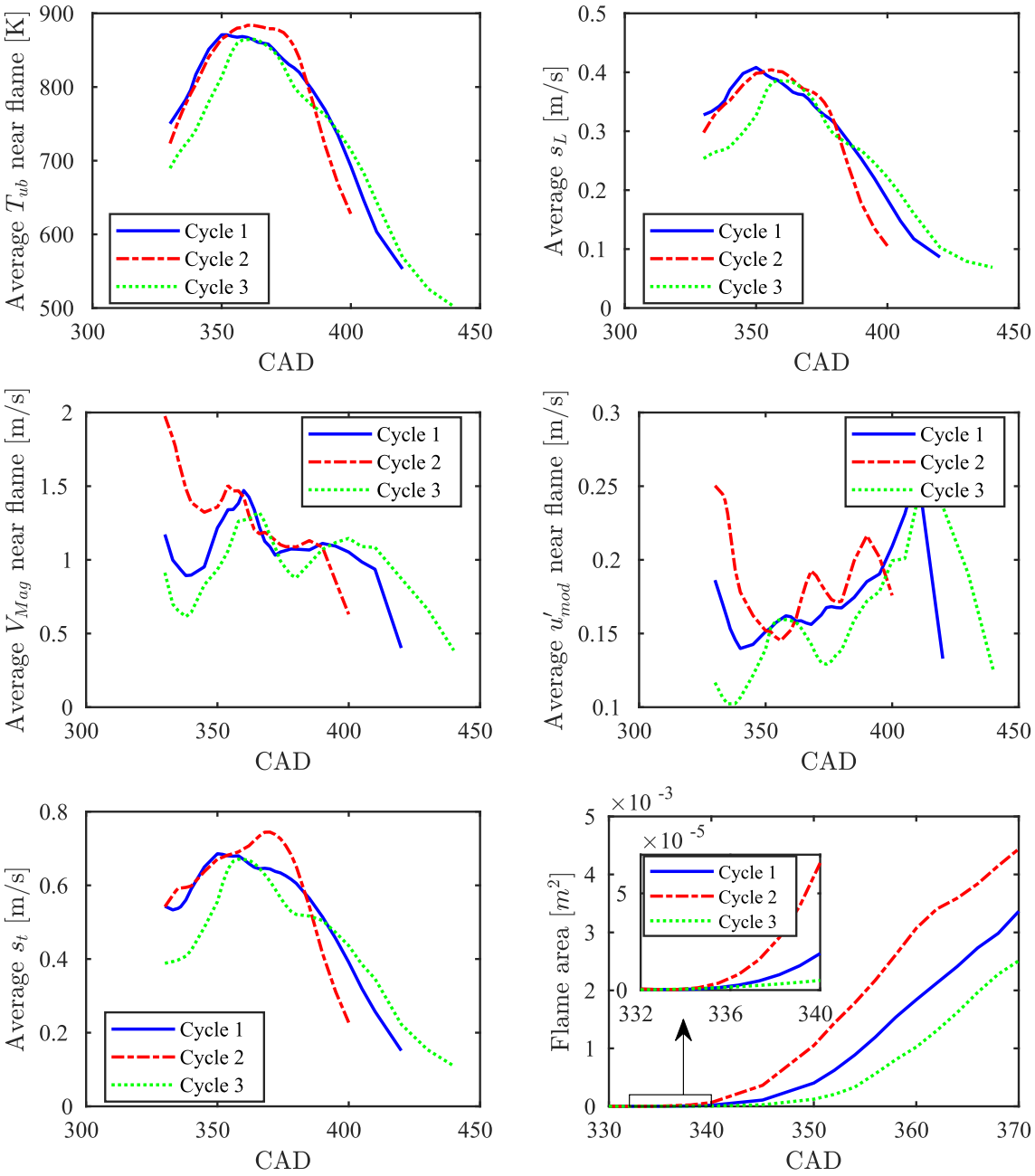

Fig. 14. Flame front metrics at 560 RPM: weighted average temperature, velocity magnitude, modeled velocity fluctuation, laminar and turbulent flame speed and early flame area (mean MFB at 370 CAD≈18%) obtained from a 4 mm band ahead of flame in the unburnt gas for the three cycles. Cycle 2 and 3 are the fastest and slowest cycles, respectively.

patterns, as will be seen later on in the paper.

Next, we investigate how local conditions in the unburnt region, right ahead of the flame, vary for the three RPM cases and different cycles. The following analysis focuses on relatively early times AST before 370 CAD. The flame front analysis is motivated by one of our leading hypotheses claiming that the initial flow conditions around the spark would largely dictate the cycle progress. We evaluate turbulence and thermal metrics within a narrow band (≈4 mm) ahead of the flame front for each RPM and cycle in order to explain the observed global cycle-to-cycle variations in combustion rate. The key metrics in the analysis are: (1) resolved velocity V_{mag}, (2) modeled velocity fluctuation u'_{mod}, (3) turbulent flame speed (s_t), (4) laminar flame speed (s_L), (5) unburnt temperature (T_{ub}), and (6) flame area.

Figs. 14–16 show the metrics for all the cases. The following general observations can be made. First, since the fuel-air mixture is nearly homogenous, s_L and temperature are strongly correlated. Second, it is noted that $V_{mag} \gg u'_{mod}$ and $V_{mag} > s_t$. Additionally, on average, V_{mag} clearly depends on RPM while s_t changes only weakly with RPM. Importantly, when going from 560 to 800, and to 1000 RPM, the average initial V_{mag} is noted to systematically increase from approximately 1.4 to 2.3, and to 3.0 m/s. Hence, the resolved velocity is expected to dominate the flame propagation modeled here in the context of the G-equation. Third, s_t is linked to s_L and u'_{mod} according to Eq. (2). Fourth, cycle-to-cycle variations in flame area clearly correlate with the respective variations of V_{mag} and s_t. Such correlation is not seen as clearly for the other metrics considered herein. Based on the general discussion above, we next focus the analysis on V_{mag}, u'_{mod}, s_t and the flame area.

At 560 RPM, Fig. 14 indicates how the initial flame kernels pose highly different initial V_{mag}, u'_{mod} and s_t. The initial differences are noted to persist between 330 and 360 CAD. For s_t the initial cycle-to-cycle

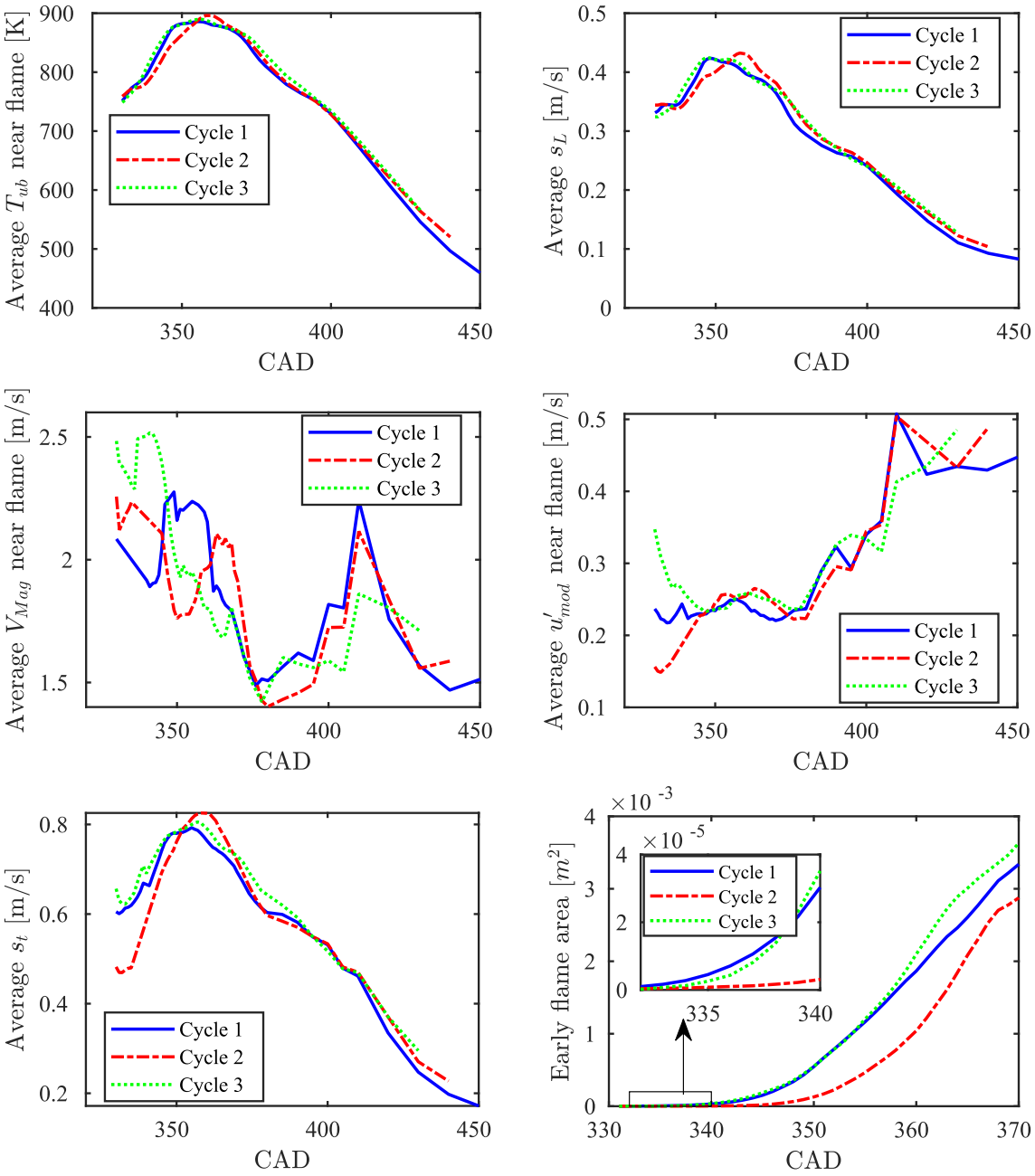

Fig. 15. Flame front metrics at 800 RPM: weighted average temperature, velocity magnitude, modeled velocity fluctuation, laminar and turbulent flame speed and early flame area (mean MFB at 370 CAD≈12%) obtained from a 4 mm band ahead of flame in the unburnt gas for the three cycles. Cycle 3 and 2 are the fastest and slowest cycles, respectively.

variation is $\delta s_t \approx 0.15$ m/s while for V_{mag} the variation is $\delta V_{mag} \approx 1$ m/s. It is noted that cycle 2 poses the highest u'_{mod} and V_{mag} compared to cycles 1 and 3, leading to the fastest flame area growth and burning rate. In Fig. 14, cycle-to-cycle variations in flame area emerge before 340 CAD i.e. very close to the spark timing. The increased flame area contributes to the total burning rate. Consequently, the cycle that burns faster initially, tends to burn faster until the end of combustion, signifying the prominent effect of local spark initial conditions on CCV.

At 800 RPM, Fig. 15 indicates how the initial flame kernels pose rather similar initial V_{mag}, u'_{mod} and s_t. Typically, the variation in these quantities is less than 0.3 m/s. This observation contrasts the 560 RPM case and the contrast will be explained later on in the paper. The initial flame area difference between the cycles is presumably due to first, u'_{mod} which led to $\delta s_t \approx 0.15$ m/s, and second, V_{mag} having $\delta V_{mag} \approx 0.3$ m/s between the cycles. The flame area growth for cycles 1 (highest V_{mag}) and 3 (highest u'_{mod}) turns out to be highly similar, while cycle 2 poses the slowest flame area growth rate which can be potentially explained by the smallest initial s_t values. It is also worth noting that V_{mag} fluctuates considerably. Thereby, we note that at 800 RPM, the flame front metrics do not pose any clear trend which would distinguish cycles 1–3 from one another. This observation is consistent with the noted small global CCV presented earlier in the paper.

At 800 RPM, the flame area of cycle 2 approaches the cycle 1 and 3 flame areas close to 370 CAD. There could be at least two explanations for such a catch-up phenomenon. First, the numerical Schlieren visualization revealed asymmetric flame evolution for cycles 1 and 3 which causes portions of the flame front to approach the lower temperature periphery of the cylinder. As the flame front reaches the wall, those parts of the flame will not contribute to the total flame area growth anymore. Second, for cycle 2, it is noted that during 360–380 CAD, V_{mag}

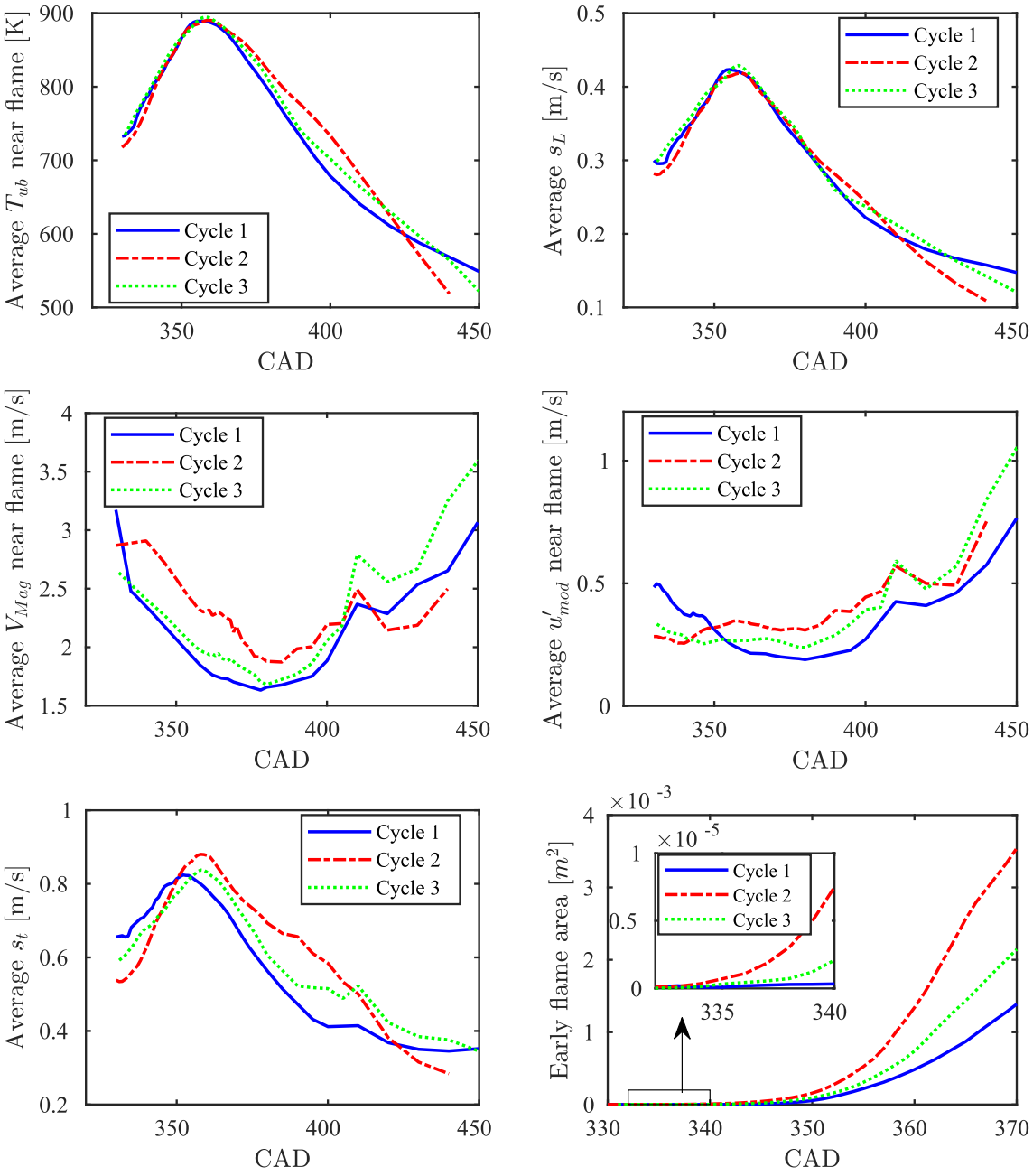

Fig. 16. Flame front metrics at 1000 RPM: weighted average temperature, velocity magnitude, modeled velocity fluctuation, laminar and turbulent flame speed and early flame area (mean MFB at 370 CAD≈5%) obtained from a 4 mm band ahead of flame in the unburnt gas for the three cycles. Cycle 2 and 1 are the fastest and slowest cycles, respectively.

levels off at similar values than cycles 1 and 3 while s_t of cycle 2 slightly exceeds cycles 1 and 3. These observations provide insight to potential causes of the catch-up phenomenon of cycle 2.

At 1000 RPM, Fig. 16 indicates how the initial flame kernels pose quite different initial V_{mag}, u'_{mod} and s_t. The initial differences are noted to persist between 330 and 400 CAD, i.e. 40 CAD longer than for the 560 RPM case. The cycle-to-cycle variations are $\delta s_t \approx 0.2$ m/s and $\delta V_{mag} \approx 0.5$ m/s. The cycle-to-cycle variations in flame area are noted to emerge before 350 CAD which is clearly later than for 560 RPM and 800 RPM cases. The provided evidence, in particular, the comparison between 560 RPM and 1000 RPM cases, indicates that for higher RPM the role of initial conditions extends to longer CAD times.

In summary, the local field analysis on the three cycles and three RPMs provided four findings as follows. (1) Turbulence and especially velocity magnitude around the early flame front largely explained the observed cycle-to-cycle variations. Large initial differences in V_{mag} resulted in large CCV (560 and 1000 RPMs), whereas initially strongly fluctuating V_{mag} (800 RPM) resulted in a very similar combustion behavior between the cycles. (2) The higher the RPM, the higher the average V_{mag} close to the spark. (3) The flame area further contributes to the total burning rate of the cycle. (4) The higher the RPM, the longer the initial effects may persist in CAD time.

3.5. Example of a lagging cycle

Next, we provide a numerical example on a low RPM cycle which is substantially lagged in CAD space in terms of a slower combustion rate than the average. Consequentially, such a lagging cycle may burn slower than a high RPM cycle contrasting the average RPM trend noted earlier. As an example, cycle 3 from 560 RPM and 800 RPM is chosen.

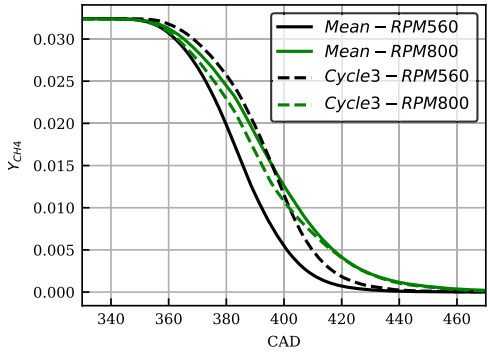

(a) Fuel mass fraction history

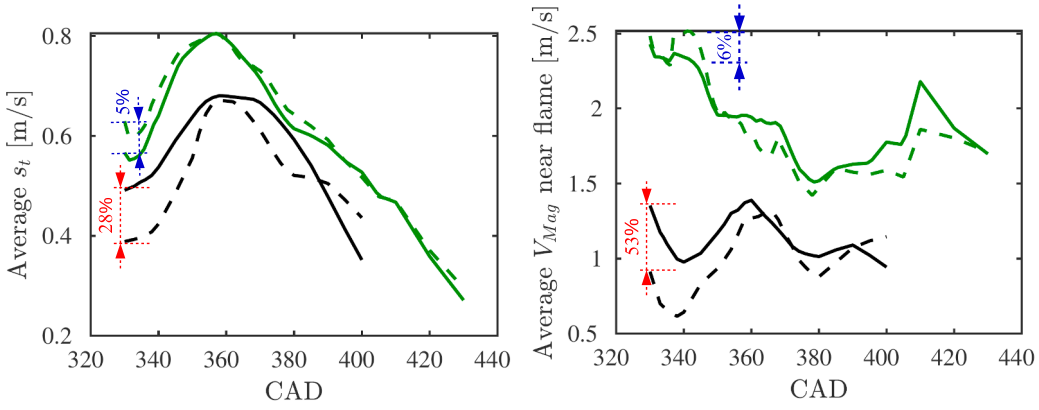

(b) Average and cycle 3 local s_t (left) and V_{mag} (right)

Fig. 17. At 560 RPM cycle 3 burns very slow in CAD time lagging the typical combustion rates of 800 RPM cases before 400 CAD. (a) Fuel mass fraction history, and (b) Average local turbulent flame speed (s_t) and resolved velocity magnitude (V_{mag}) at 560 and 800 RPM.

As discussed earlier in Fig. 6, high RPM indicates longer mean combustion duration in CAD space. Although high RPM cases feature slightly higher s_t and significantly higher V_{mag} values than low RPM cases, they have less physical time available for flame propagation. However, the following example shows that contradictions to this average behavior may exist. In particular, Fig. 17(a) shows that the slow burning cycle 3 at 560 RPM exceeds the combustion phasing of both the mean and cycle 3 from 800 RPM for a substantial part of the combustion duration and in particular before 390 CAD.

To explain such a lagging character, Fig. 17(b) shows a comparison between average s_t and V_{mag} for cycles 3 and the mean cycles at 560 and 800 RPM. It is observed that at 800 RPM, cycle 3 follows rather closely the mean cycle in terms of the both average V_{mag} and s_t metrics (within 2–6%). In contrast, at 560 RPM, cycle 3 is clearly slower than the mean cycle in terms of the two metrics, the difference being between 28 and 53%. This analysis demonstrates that cycle 3 at 560 RPM is an extremely slow cycle mainly due to low V_{mag} over initial CAD time instances, which denotes the importance of V_{mag} over initial CAD time instances in swapping the order of combustion phasing.

4. Discussion

Next, we would like to comment on the different modeling assumptions and limitations made in the chosen modeling avenue. First, in order to isolate the engine speed impact from any other effects, the spark timing was set to constant which is in contrast to typical engine practices. Second, the present results were validated only in non-reacting conditions at low RPM. However, the noted low ratio of modeled and physical viscosities in Fig. 4 supports the assumption of relatively well resolved flow also for the higher RPM cases. Third, the initial spark size is rather small in the studied cases, which makes it more prone to local conditions [24]. Fourth, the observed combustion trends are conditional on the turbulent flame speed model by Muppala [49] which shows rather weak dependency on turbulence and RPM.

From modeling perspective, the core challenge in future studies is to balance the trade-off between the very high computational burden of scale-resolved simulations and the extraction of information on cycle-to-cycle variations i.e. repetition of multiple engine cycles. In this regard, a practical avenue for studying CCVs in SI engine context would be to use only a few cycles as BDC initial conditions and to recycle/superimpose the data for emulating different initial conditions near the spark. Such an approach would greatly ease the computational efforts for studying CCVs. Also, local flame analysis at early time instances (where the kernel is small) was shown to be an effective approach to capture the combustion CCV. Last, a proper wall-modeling strategy, such as the HLR-WT model utilized herein, is considered to be highly useful for computational speed-up.

From engine practitioners perspective, one of the core challenges is to minimize the CCV for different operating conditions. First, from the viewpoint of low-speed engines, RPM is commonly fixed to provide the desired power output. To reduce CCV, the spark timing needs to be optimized. The present simulations motivate such optimization and control strategies because the relative duration of any initial effects in CAD time can be potentially made smaller. Second, it was observed that the studied small kernels can be substantially affected by local flow magnitude around the spark. Therefore, a larger/stronger kernel may reduce the early kernel proneness to local field variations. Third, the stabilization of the early flow conditions, such as tumble or swirl, near

the spark may be crucial for controlling CCV. In this aspect, techniques such as pre-chamber ignition can be extremely useful.

5. Conclusions

Here, scale-resolving simulations along with the G-equation combustion model were used to investigate engine RPM effects. The study provided insight to the origins of CCVs in lean burn SI engine context. To address objectives of the study, three different engine speeds were investigated for three separate cycles leading to the following conclusions.

1. Increased RPM was noted to increase flow velocity and turbulence levels during the compression phase due to increased mean piston speed. However, turbulent flame speed was noted to scale only weakly on RPM consistent with the utilized turbulent flame speed model.
2. For a fixed spark timing, higher RPM was noted to decrease the mean combustion duration in physical time while in CAD space the combustion duration increased. Compared to 560 RPM, the flame speed of the mean cycle at early time instances after spark time increased 16% at 800 RPM and 23% at 1000 RPM. However, the increased turbulent flame speed was relatively minute and could not compensate the respective 42 and 78% reduced physical time for flame development.
3. The low CCV at 800 RPM was explained by the flame front analysis where no specific trend was seen as the velocity metrics fluctuated in an overlapping manner at early times after spark time (up to 370 CAD) for cycles 1–3. In addition, the asymmetric flame propagation of cycles 1 and 3 pushed them towards colder cylinder periphery, where cycle 2 showed an increased T and s_t compared to the other two cycles.
4. The flame front analysis revealed that the initial differences in turbulent flame speed (s_t) and resolved velocity magnitudes (V_{mag}) between the cycles largely described the early changes in the flame area, and CCV. In addition, with relatively low composition stratification, V_{mag} had a major contribution to the observed CCV.
5. Early signs of CCVs appeared already during the first 10 CADs after spark timing in all the studied cases. It was also noted that local variations are much more influential when the flame kernel is small in all engine speeds.
6. Increasing engine speed extends the CAD time period in which flame kernel is small and still susceptible to local field variations.

In this study, the spark timing was fixed to 30CAD BTDC. As stated before, it is a common practice to advance the spark timing at higher speeds. Therefore, considering different spark timings at higher engine speeds and indicating its influence on CCV can be considered as a research pathway for future studies.

Acknowledgement

The present study has been supported by the Aalto University Graduate School, Wärtsilä Co., and Academy of Finland (Grant Nos. 318024 and 289592). We acknowledge the computational resources provided by the Aalto Science-IT project.

Appendix A. Laminar flame speed correlation

The implemented laminar flame speed correlation in the present study is described as follows. The present model is provided for conditions spanned by T = 400–950 K, fuel to air equivalence ratios = 0.45–1.1 and P = 1–50 bar (see Tables A.1–A.3)

Table A.1
Division of temperature and composition fields for the present s_L correlation.

Region 1	Region 2	Region 3
$400 < T \leqslant 650$ $0.45 \leqslant \phi \leqslant 0.5$	$400 < T \leqslant 650$ $0.5 < \phi \leqslant 0.7$	$400 < T \leqslant 650$ $0.7 < \phi \leqslant 1.1$
Region 4	Region 5	Region 6
$650 < T \leqslant 950$ $0.45 \leqslant \phi \leqslant 0.5$	$650 < T \leqslant 950$ $0.5 < \phi \leqslant 0.7$	$650 < T \leqslant 950$ $0.7 < \phi \leqslant 1.1$

Table A.2
The present s_L coefficients for different regions.

	Regions					
Coefficient	Region 1	Region 2	Region 3	Region 4	Region 5	Region 6
c1	−5.3194	−1.0863	−3.2726	78.4840	25.8019	0.8999
c2	1.2173	1.1442	1.0555	50.7748	17.6897	2.7202
c3	−0.6626	−0.5757	−0.4547	−0.6297	−0.4966	−0.3806
c4	0.1298	0.0655	0.0223	0.1242	0.0308	−0.0119
c5	5.5042	3.9316	2.6138	−121.8737	−38.2551	−1.4444
c6	−1.1016	−0.6573	−0.2865	39.5021	12.6720	0.9723
c7	2.8581	4.4202	2.6064	0.1855	2.1634	2.1985
c8	8.0830	1.8639	5.4718	10.6310	3.2106	2.4332
c9	−5.8585	−2.9771	−3.7677	−6.0912	−2.6120	−2.1050

Table A.3
The present laminar flame speed performance in different regions.

Regions	Error		
	Maximum Error	Mean Error	L2 Error
Region 1	0.0942	0.0223	0.0383
Region 2	0.1360	0.0288	0.0543
Region 3	0.1929	0.0279	0.0613
Region 4	0.1993	0.0535	0.0762
Region 5	0.1883	0.0391	0.0613
Region 6	0.2647	0.0321	0.0711

$$s_L = \exp(c \cdot A^T), \text{ where}$$
$$c = [c_1, c_2, c_3, c_4, c_5, c_6, c_7, c_8, c_9],$$
$$A = \left[1, \log(T_f), \log(P_f), P_f, T_f, T_f^2, \log(\phi_f), \phi_f, \phi_f^2\right],$$
$$T_f = T/1000, \quad P_f = P/10^6, \quad \phi_f = \phi, \tag{A.1}$$

Appendix B. Global statistics of velocity magnitude

Cycle-to-cycle variation in cell-volume weighted PDFs of resolved velocity magnitude from the unburnt region is demonstrated in Fig. B.1. It is observed that at any CAD for either 560 or 800 RPM, there are no significant differences in the probabilities of the V_{mag} among the cycles implying global statistical similarity. For 1000 RPM, the upper tail of the PDF shows more deviation between the cycles during the compression in the unburnt end-gas region. At 1000 RPM, it is noted that cycle 2 with the highest and cycle 1 with the lowest probability of high V_{mag} also represent the fastest and slowest cycles, respectively (see Fig. 9).

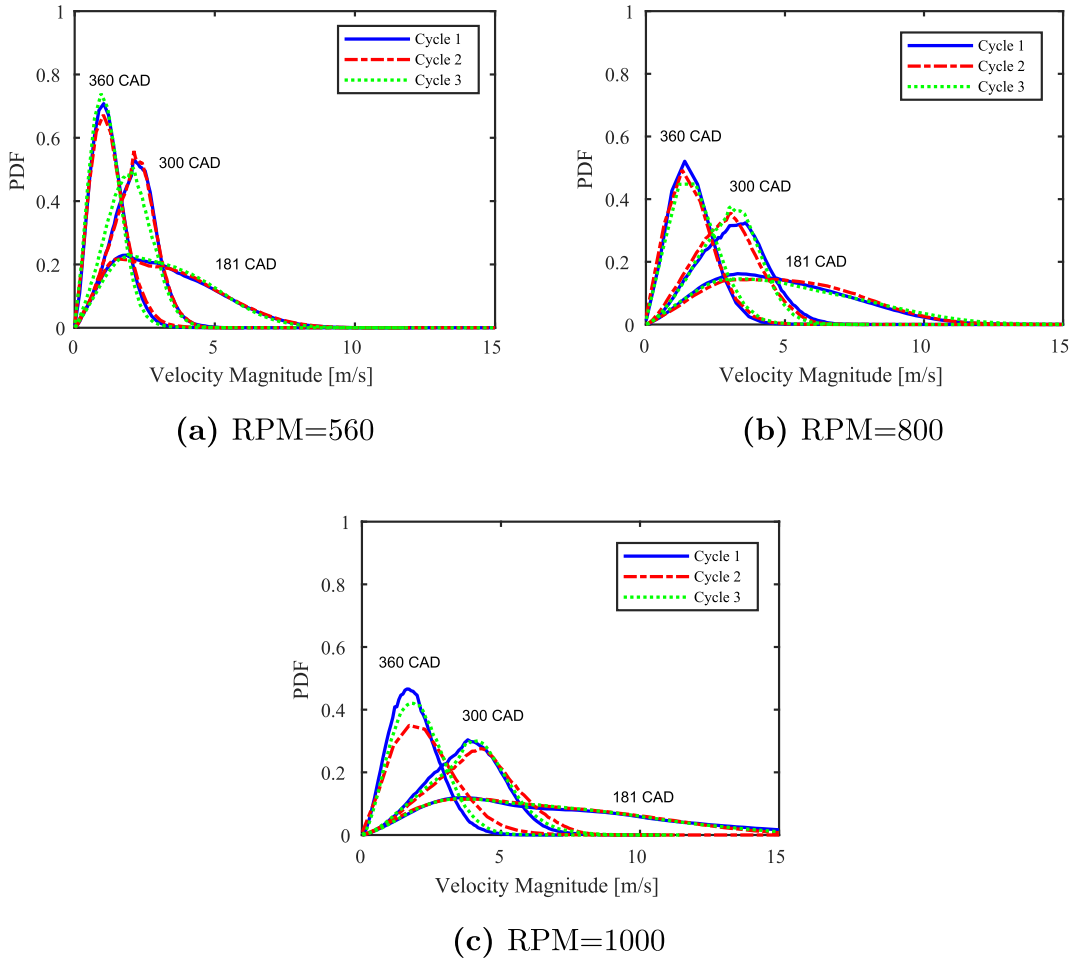

Fig. B.1. The resolved velocity magnitude PDFs from the unburnt region during compression in the unburnt end-gas at (a) 560 RPM, (b) 800 RPM and (c) 1000 RPM. The higher the RPM, the higher the average velocities and the broader the velocity PDFs.

References

[1] ©OECD/IEA. International Energy Agency: World Energy Outlook 2018; 2018. <https://www.iea.org/weo/>.

[2] ©OECD/IEA. International Energy Agency: Energy Technology Perspectives 2014, Tech. Rep.; 2014.

[3] Finney CE, Kaul BC, Daw CS, Wagner RM, Edwards KD, Green JB. Invited review: a review of deterministic effects in cyclic variability of internal combustion engines. Int J Engine Res 2015;16(3):366–78. https://doi.org/10.1177/1468087415572033. ISSN 1468-0874 <http://journals.sagepub.com/doi/10.1177/1468087415572033> .

[4] Cho HM, He BQ. Spark ignition natural gas engines – a review. Energy Convers Manage 2007;48(2):608–18. https://doi.org/10.1016/j.enconman.2006.05.023. ISSN 01968904 <http://linkinghub.elsevier.com/retrieve/pii/S0196890406001919> .

[5] Jung D, Sasaki K, Iida N. Effects of increased spark discharge energy and enhanced in-cylinder turbulence level on lean limits and cycle-to-cycle variations of combustion for SI engine operation. Appl Energy 2017;205:1467–77. https://doi.org/10.1016/j.apenergy.2017.08.043. ISSN 0306-2619 <http://www.sciencedirect.com/science/article/pii/S0306261917310590> .

[6] Lee S, Park S, Kim C, Kim Y-M, Kim Y, Park C. Comparative study on EGR and lean burn strategies employed in an SI engine fueled by low calorific gas. Appl Energy 2014;129:10–6. https://doi.org/10.1016/j.apenergy.2014.04.082. ISSN 0306-2619 <http://www.sciencedirect.com/science/article/pii/S0306261914004450> .

[7] Kim K, Kim J, Oh S, Kim C, Lee Y. Evaluation of injection and ignition schemes for the ultra-lean combustion direct-injection LPG engine to control particulate emissions. Appl Energy 2017;194:123–35. https://doi.org/10.1016/j.apenergy.2017.03.012. ISSN 0306-2619 <http://www.sciencedirect.com/science/article/pii/S0306261917302271> .

[8] Kyrtatos P, Brückner C, Boulouchos K. Cycle-to-cycle variations in diesel engines. Appl Energy 2016;171:120–32. https://doi.org/10.1016/j.apenergy.2016.03.015. ISSN 0306-2619 <http://www.sciencedirect.com/science/article/pii/S0306261916303269> .

[9] Maurya RK, Agarwal AK. Experimental investigation on the effect of intake air temperature and air–fuel ratio on cycle-to-cycle variations of HCCI combustion and performance parameters. Appl Energy 2011;88(4):1153–63. https://doi.org/10.1016/j.apenergy.2010.09.027. ISSN 0306-2619 <http://www.sciencedirect.com/science/article/pii/S0306261910003922> .

[10] Badawy T, Bao X, Xu H. Impact of spark plug gap on flame kernel propagation and engine performance. Appl Energy 2017;191:311–27. https://doi.org/10.1016/j.apenergy.2017.01.059. ISSN 0306-2619 <http://www.sciencedirect.com/science/article/pii/S0306261917300673> .

[11] Maurya RK, Agarwal AK. Experimental study of combustion and emission characteristics of ethanol fuelled port injected homogeneous charge compression ignition (HCCI) combustion engine. Appl Energy 2011;88(4):1169–80. https://doi.org/10.1016/j.apenergy.2010.09.015. ISSN 0306-2619 <http://www.sciencedirect.com/science/article/pii/S0306261910003806> .

[12] Ozdor N, Dulger M, Sher E. Cyclic variability in spark ignition engines a literature survey, SAE Technical Paper 940987; 1994. Warrendale, PA: SAE International. <http://papers.sae.org/940987/>.

[13] Johansson B. Cycle to cycle variations in S.I. engines - the effects of fluid flow and gas composition in the vicinity of the spark plug on early combustion. In: SAE Technical Paper 962084, ISSN 0148-7191; 1996. doi:https://doi.org/10.4271/962084, <http://papers.sae.org/962084/>.

[14] Reyes M, Tinaut FV, Giménez B, Pérez A. Characterization of cycle-to-cycle variations in a natural gas spark ignition engine. Fuel 2015;140:752–61. https://doi.org/10.1016/j.fuel.2014.09.121. ISSN 0016-2361 <http://www.sciencedirect.com/science/article/pii/S0016236114009971> .

[15] Reuss DL. Cyclic variability of large-scale turbulent structures in directed and undirected IC engine flows, SAE Technical Paper 2000-01-0246, 2000. Warrendale, PA: SAE International. doi:https://doi.org/10.4271/2000-01-0246. <https://www.sae.org/publications/technical-papers/content/2000-01-0246/>.

[16] Koch J, Schmitt M, Wright YM, Steurs K, Boulouchos K. LES multi-cycle analysis of the combustion process in a small SI engine. SAE Int J Engines 2014;7(1):269–85. https://doi.org/10.4271/2014-01-1138. ISSN 1946-3944 <http://papers.sae.org/2014-01-1138/> .

[17] Truffin K, Angelberger C, Richard S, Pera C. Using large-eddy simulation and multivariate analysis to understand the sources of combustion cyclic variability in a spark-ignition engine. Combust Flame 2015;162(12):4371–90. https://doi.org/10.1016/j.combustflame.2015.07.003. ISSN 0010-2180 <http://www.sciencedirect.com/science/article/pii/S0010218015002047> .

[18] Pan J, Wei H, Shu G, Pan M, Feng D, Li N. LES analysis for auto-ignition induced abnormal combustion based on a downsized SI engine. Appl Energy 2017;191:183–92. https://doi.org/10.1016/J.APENERGY.2017.01.044. ISSN 0306-2619 <https://www.sciencedirect.com/science/article/pii/S0306261917300521?via%3Dihub> .

[19] Kodavasal J, Moiz AA, Ameen M, Som S. Using machine learning to analyze factors determining cycle-to-cycle variation in a spark-ignited gasoline engine. J Energy Resour Technol. ISSN 0195-0738, doi:https://doi.org/10.1115/1.4040062.

[20] Ameen MM, Mirzaeian M, Millo F, Som S. Numerical prediction of cyclic variability in a spark ignition engine using a parallel large eddy simulation approach. J Energy Res Technol 2018;140(5). https://doi.org/10.1115/1.4039549. 052203–052203–10, ISSN 0195-0738.

[21] D'Adamo A, Breda S, Berni F, Fontanesi S. Understanding the origin of cycle-to-cycle variation using large-eddy simulation: similarities and differences between a homogeneous low-revving speed research engine and a production DI turbocharged engine. SAE Int J Engines 2018;12(1). https://doi.org/10.4271/03-12-01-0007. 03–12–01–0007, ISSN 1946-3944 <https://www.sae.org/content/03-12-01-0007/> .

[22] Chen C, Ameen MM, Wei H, Iyer C, Ting F, Vanderwege B, et al. LES analysis on cycle-to-cycle variation of combustion process in a DISI Engine. In: SAE Technical Paper 2019-01-0006; 2019. ISSN 0148-7191, doi:https://doi.org/10.4271/2019-01-0006. <https://www.sae.org/content/2019-01-0006/>.

[23] Fontanesi S, D'Adamo A, Rutland CJ. Large-Eddy simulation analysis of spark configuration effect on cycle-to-cycle variability of combustion and knock. Int J Engine Res 2015;16(3):403–18. https://doi.org/10.1177/1468087414566253. ISSN 1468-0874 <http://journals.sagepub.com/doi/10.1177/1468087414566253> .

[24] Ghaderi Masouleh M, Keskinen K, Kaario O, Kahila H, Wright YM, Vuorinen V. Flow and thermal field effects on cycle-to-cycle variation of combustion: scale-resolving simulation in a spark ignited simplified engine configuration. Appl Energy 2018;230:486–505. https://doi.org/10.1016/j.apenergy.2018.08.046. ISSN 0306-2619 <http://www.sciencedirect.com/science/article/pii/S0306261918312017> .

[25] Aleiferis PG, Taylor AMKP, Whitelaw JH, Ishii K, Urata Y. Cyclic variations of initial flame kernel growth in a Honda VTEC-E lean-burn spark-ignition engine. In: SAE Technical Paper 2000-01-1207; 2000. ISSN 0148-7191, doi:https://doi.org/10.4271/2000-01-1207. <http://papers.sae.org/2000-01-1207/>.

[26] Liu J, Dumitrescu CE. Flame development analysis in a diesel optical engine converted to spark ignition natural gas operation. Appl Energy 2018;230:1205–17. https://doi.org/10.1016/J.APENERGY.2018.09.059. ISSN 0306-2619 <https://www-sciencedirect-com.libproxy.aalto.fi/science/article/pii/S0306261918313679> .

[27] Ko I, Min K, Fontanesi S, Rulli F, Ha T, Choi H. Impact of grid density on the LES analysis of flow CCV: application to the TCC-III engine under motored conditions. In: SAE Technical Paper 2018-01-0203; 2018, ISSN 0148-7191. doi:https://doi.org/10.4271/2018-01-0203. <http://www.sae.org/content/2018-01-0203/>.

[28] Keskinen K, Koch J, Wright YM, Schmitt M, Nuutinen M, Kaario O, et al. Numerical assessment of wall modelling approaches in scale-resolving in-cylinder simulations. Int J Heat Fluid Flow 2018;74:154–72. https://doi.org/10.1016/j.ijheatfluidflow.2018.09.016. ISSN 0142-727X <http://www.sciencedirect.com/science/article/pii/S0142727X1830002X> .

[29] Schmitt M, Frouzakis CE, Wright YM, Tomboulides AG, Boulouchos K. Investigation of wall heat transfer and thermal stratification under engine-relevant conditions using DNS. Int J Engine Res 2016;17(1):63–75. https://doi.org/10.1177/1468087415588710. ISSN 1468-0874.

[30] Schmitt M, Frouzakis CE, Wright YM, Tomboulides AG, Boulouchos K. Direct numerical simulation of the compression stroke under engine-relevant conditions: Evolution of the velocity and thermal boundary layers. Int J Heat Mass Transf 2015;91:948–60. https://doi.org/10.1016/j.ijheatmasstransfer.2015.08.031. ISSN 0017-9310 <http://www.sciencedirect.com/science/article/pii/S001793101500873X> .

[31] Schmitt M, Frouzakis CE, Tomboulides AG, Wright YM, Boulouchos K. Direct numerical simulation of the effect of compression on the flow, temperature and composition under engine-like conditions. Proc Combust Inst 2015;35(3):3069–77. https://doi.org/10.1016/j.proci.2014.06.097. ISSN 1540-7489 <http://www.sciencedirect.com/science/article/pii/S1540748914002557> .

[32] Nuutinen MA, Kaario OT, Vuorinen VA, Nwosu PN, Larmi MJ. Imbalance wall functions with density and material property variation effects applied to engine heat transfer computational fluid dynamics simulations. Int J Engine Res 2014;15(3):307–24. https://doi.org/10.1177/1468087413481779. ISSN 1468-0874.

[33] Keskinen K, Nuutinen M, Kaario O, Vuorinen V, Koch J, Wright YM, et al. Hybrid LES/RANS with wall treatment in tangential and impinging flow configurations. Int J Heat Fluid Flow 2017;65:141–58. https://doi.org/10.1016/j.ijheatfluidflow.2017.04.001. ISSN 0142-727X <http://www.sciencedirect.com/science/article/pii/S0142727X16306452> .

[34] Williams FA. Combustion theory (combustion science and engineering); 1985.

[35] Young MB. Cyclic dispersion in the homogeneous-charge spark-ignition engine—a literature survey, SAE Technical Paper 810020; 1981. Warrendale, PA: SAE International. doi:https://doi.org/10.4271/810020. <https://www.sae.org/publications/technical-papers/content/810020/>.

[36] Aydin K. Effect of engine parameters on cyclic variations in spark ignition engines. In: International Advanced Technologies Symposium (IATS'11), 7.

[37] Huang B, Hu E, Huang Z, Zheng J, Liu B, Jiang D. Cycle-by-cycle variations in a spark ignition engine fueled with natural gas–hydrogen blends combined with EGR. Int J Hydrogen Energy 2009;34(19):8405–14. https://doi.org/10.1016/j.ijhydene.2009.08.002. ISSN 0360-3199 <http://www.sciencedirect.com/science/article/pii/S0360319909012440> .

[38] Sen AK, Zheng J, Huang Z. Dynamics of cycle-to-cycle variations in a natural gas direct-injection spark-ignition engine. Appl Energy 2011;88(7):2324–34. https://doi.org/10.1016/j.apenergy.2011.01.009. ISSN 0306-2619 <http://www.sciencedirect.com/science/article/pii/S0306261911000122> .

[39] Nicoud F, Toda HB, Cabrit O, Bose S, Lee J. Using singular values to build a subgrid-scale model for large eddy simulations. Phys Fluids 2011;23(8):085106. https://doi.org/10.1063/1.3623274. ISSN 1070-6631 <http://aip.scitation.org/doi/abs/10.1063/1.3623274> .

[40] Dahms R, Fansler TD, Drake MC, Kuo TW, Lippert AM, Peters N. Modeling ignition phenomena in spray-guided spark-ignited engines. Proc Combust Inst

2009;32(2):2743–50. https://doi.org/10.1016/j.proci.2008.05.052. ISSN 1540-7489 <http://www.sciencedirect.com/science/article/pii/S1540748908002587> .
[41] Liu J, Dumitrescu CE. 3D CFD simulation of a CI engine converted to SI natural gas operation using the G-equation. Fuel 2018;232:833–44. https://doi.org/10.1016/j.fuel.2018.05.159. ISSN 0016-2361 <http://www.sciencedirect.com/science/article/pii/S0016236118310044> .
[42] Pitsch H, Duchamp de Lageneste L. Large-eddy simulation of premixed turbulent combustion using a level-set approach. Proc Combust Inst 2002;29(2):2001–8. https://doi.org/10.1016/S1540-7489(02)80244-9. ISSN 15407489 <http://linkinghub.elsevier.com/retrieve/pii/S1540748902802449> .
[43] Charlette F, Meneveau C, Veynante D. A power-law flame wrinkling model for LES of premixed turbulent combustion Part I: non-dynamic formulation and initial tests. Combust Flame 2002;131(1–2):159–80. https://doi.org/10.1016/S0010-2180(02)00400-5. ISSN 00102180 <http://linkinghub.elsevier.com/retrieve/pii/S0010218002004005> .
[44] Colin O, Ducros F, Veynante D, Poinsot T. A thickened flame model for large eddy simulations of turbulent premixed combustion. Phys Fluids 2000;12(7):1843–63. https://doi.org/10.1063/1.870436. ISSN 1070-6631 <http://aip.scitation.org/doi/10.1063/1.870436> .
[45] Fureby C. A fractal flame-wrinkling large eddy simulation model for premixed turbulent combustion. Proc Combust Inst 2005;30(1):593–601. https://doi.org/10.1016/j.proci.2004.08.068. ISSN 15407489 <http://linkinghub.elsevier.com/retrieve/pii/S0082078404001316> .
[46] Knikker R, Veynante D, Meneveau C. A dynamic flame surface density model for large eddy simulation of turbulent premixed combustion. Phys Fluids 2004;16(11):L91–4. https://doi.org/10.1063/1.1780549. ISSN 1070-6631, 1089-7666 <http://aip.scitation.org/doi/10.1063/1.1780549> .
[47] Tangermann E, Keppeler R, Pfitzner M. Premixed turbulent combustion models for large Eddy and RANS simulations; 2010. p. 203–12. doi:https://doi.org/10.1115/GT2010-22298.
[48] Weller HG, Tabor G, Gosman AD, Fureby C. Application of a flame-wrinkling les combustion model to a turbulent mixing layer. Symp (Int) Combust 1998;27(1):899–907. https://doi.org/10.1016/S0082-0784(98)80487-6. ISSN 0082-0784 <http://www.sciencedirect.com/science/article/pii/S0082078498804876> .
[49] Muppala SR, Aluri NK, Dinkelacker F, Leipertz A. Development of an algebraic reaction rate closure for the numerical calculation of turbulent premixed methane, ethylene, and propane/air flames for pressures up to 1.0 MPa. Combust Flame 2005;140(4):257–66. https://doi.org/10.1016/j.combustflame.2004.11.005. ISSN 00102180 <http://linkinghub.elsevier.com/retrieve/pii/S0010218004002329> .
[50] Ma T, Stein OT, Chakraborty N, Kempf AM. A posteriori testing of algebraic flame surface density models for LES. Combust Theor Model 2013;17(3):431–82. https://doi.org/10.1080/13647830.2013.779388. ISSN 1364-7830.
[51] Burke EM, Güthe F, Monaghan RFD. A comparison of turbulent flame speed correlations for hydrocarbon fuels at elevated pressures; 2016. p. V04BT04A043. doi:https://doi.org/10.1115/GT2016-57804.
[52] Gulder OL. Turbulent premixed flame propagation models for different combustion regimes. Symp (Int) Combust 1991;23(1):743–50. https://doi.org/10.1016/S0082-0784(06)80325-5. ISSN 0082-0784 <http://www.sciencedirect.com/science/article/pii/S0082078406803255> .
[53] Amirante R, Distaso E, Tamburrano P, Reitz RD. Laminar flame speed correlations for methane, ethane, propane and their mixtures, and natural gas and gasoline for spark-ignition engine simulations. Int J Engine Res 2017;18(9):951–70. https://doi.org/10.1177/1468087417720018. ISSN 1468-0874.
[54] Amirante R, Distaso E, Tamburrano P, Reitz RD. Analytical correlations for modeling the laminar flame speed of natural gas surrogate mixtures. Energy Procedia 2017;126:850–7. https://doi.org/10.1016/j.egypro.2017.08.289. ISSN 1876-6102 <http://www.sciencedirect.com/science/article/pii/S1876610217337955> .
[55] Cantera. Object-oriented software tool: Documentation version 2.2.1; 2016. <http://www.cantera.org/docs/sphinx/html/index.html>, bibtex: _cantera.
[56] G.-M. 3.0, A mechanism for methane combustion; 2000. <http://www.me.berkeley.edu/gri_mech/>.
[57] Ghaderi Masouleh M, Wehrfritz A, Kaario O, Kahila H, Vuorinen V. Comparative study on chemical kinetic schemes for dual-fuel combustion of n-dodecane/methane blends. Fuel 2017;191:62–76. https://doi.org/10.1016/j.fuel.2016.10.114. ISSN 0016-2361 <http://www.sciencedirect.com/science/article/pii/S001623611631078X> .
[58] Peters N. Turbulent combustion. Cambridge University Press; 2000. ISBN 978-1-139-42806-4.
[59] Abdel-Gayed RG, Bradley D. A two-eddy theory of premixed turbulent flame propagation. Phil Trans R Soc Lond A 1981;301(1457):1–25. https://doi.org/10.1098/rsta.1981.0096. ISSN 0080-4614, 2054-0272 <http://rsta.royalsocietypublishing.org/content/301/1457/1> .
[60] Chakraborty N, Klein M. A priori direct numerical simulation assessment of algebraic flame surface density models for turbulent premixed flames in the context of large eddy simulation. Phys Fluids 2008;20(8):085108. https://doi.org/10.1063/1.2969474. ISSN 1070-6631 <https://aip.scitation.org/doi/10.1063/1.2969474> .
[61] Katragadda M, Chakraborty N, Cant RS. Effects of turbulent reynolds number on the performance of algebraic flame surface density models for large Eddy simulation in the thin reaction zones regime: a direct numerical simulation analysis. J Combust 2012: 2012:1–13, ISSN 2090-1968, 2090-1976. doi:https://doi.org/10.1155/2012/353257. <http://www.hindawi.com/journals/jc/2012/353257/>.
[62] Katragadda M, Chakraborty N, Cant RS. A priori assessment of algebraic flame surface density models in the context of large Eddy simulation for nonunity lewis number flames in the thin reaction zones regime. J Combust 2012; 2012:1–17, ISSN 2090-1968, 2090-1976. doi:https://doi.org/10.1155/2012/794671. <http://www.hindawi.com/journals/jc/2012/794671/>.
[63] Granet V, Vermorel O, Lacour C, Enaux B, Dugué V, Poinsot T. Large-Eddy Simulation and experimental study of cycle-to-cycle variations of stable and unstable operating points in a spark ignition engine. Combust Flame 2012;159(4):1562–75. https://doi.org/10.1016/j.combustflame.2011.11.018. ISSN 0010-2180 <http://www.sciencedirect.com/science/article/pii/S0010218011003920> .
[64] Fontana G, Galloni E. Experimental analysis of a spark-ignition engine using exhaust gas recycle at WOT operation. Appl Energy 2010;87(7):2187–93 <https://ideas.repec.org/a/eee/appene/v87y2010i7p2187-2193.html> .
[65] Morse AP, Whitelaw JH, Yianneskis M. Turbulent flow measurements by laser-doppler anemometry in motored piston-cylinder assemblies. J Fluids Eng 1979;101(2):208. https://doi.org/10.1115/1.3448937. ISSN 00982202 <http://FluidsEngineering.asmedigitalcollection.asme.org/article.aspx?articleid=1424634> .
[66] Nguyen TM, Proch F, Wlokas I, Kempf AM. Large Eddy Simulation of an internal combustion engine using an efficient immersed boundary technique. Flow, Turbul Combust 2016;97(1):191–230. https://doi.org/10.1007/s10494-015-9683-4. ISSN 1573-1987.
[67] Celik IB, Cehreli ZN, Yavuz I. Index of resolution quality for Large Eddy Simulations. J Fluids Eng 2005;127(5):949–58. https://doi.org/10.1115/1.1990201. ISSN 0098-2202.
[68] Nguyen TM, Proch F, Wlokas I, Kempf AM. Large Eddy Simulation of an internal combustion engine using an efficient immersed boundary technique. Flow Turbul Combust 2015;97(1):191–230. https://doi.org/10.1007/s10494-015-9683-4. ISSN 1386-6184, 1573-1987 <http://link.springer.com/article/10.1007/s10494-015-9683-4> .
[69] Keskinen J-P, Vuorinen V, Kaario O, Larmi M. Large eddy simulation of a piston–cylinder assembly: the sensitivity of the in-cylinder flow field for residual intake and in-cylinder velocity structures. Comput Fluids 2015;122:123–35. https://doi.org/10.1016/j.compfluid.2015.08.028. ISSN 0045-7930 <http://www.sciencedirect.com/science/article/pii/S0045793015003047> .